ENGINEERING THE RESONANCES OF TERHERTZ METAMATERIALS

BY

RANJAN SINGH

Bachelor of Engineering
Bangalore University,
Bangalore, India.
2001

Master of Technology
Cochin University of Science and Technology,
Kochi, Kerala, India.
2004

Submitted to the Faculty of the
Graduate College of
Oklahoma State University
in partial fulfillment of
the requirements for
the Degree of
DOCTOR OF PHILOSOPHY
December, 2009

ENGINEERING THE RESONANCES OF TERHERTZ METAMATERIALS

Dissertation Approved:

Dr. Weili Zhang

Dissertation Adviser

Dr. R. A. Cheville

Dr. Daqing Piao

Dr. G. S. Agarwal

Dr. James P. Wicksted

Dr. A. Gordon Emslie

Dean of the Graduate College

ACKNOWLEDGEMENTS

I would like to thank my adviser Dr. Weili Zhang for accepting me as his PhD student at a time when I was almost branded as a student completely incapable of doing research. He introduced me to the fascinating world of metamaterials and successfully guided me through my research. His tremendous faith in my abilities and unwavering support inspired me to work hard and work smart. I enjoyed all the freedom he gave me to do my work. I can hardly remember a situation where I would discuss an experiment or an idea with him and he showed any lack of confidence in it. The best thing I liked about him is that he was always there in the encouraging role every time I needed his inputs or any kind of assistance in the laboratory. Thanks for being so Dr. Zhang, I really appreciate all your patience, faith and support.

Dr. Paul Westhaus, then (August 2006) the Photonics program director provided me with the financial support through the Department of Physics without which I would not have been able to survive here and thus would not have continued my PhD. Thanks a lot Dr. Westhaus for showing so much trust in my abilities. If it was not your generosity, I would have faded into oblivion several years back without making any kind of impact in the research arena and would have probably sulked all my life thinking that I failed miserably to even get close to earning that dream degree called "PhD" for which I came to America.

I would like to thank Dr. Tae-In Jeon and Dr. Norman Laman, the two postdocs and a senior colleague Dr. Mufei Gong who trained me with basic experimental techniques. Dr. Abul K. Azad was always an instant help to me whenever I struggled in the lab. He always motivated me and showed the right path every time I felt low during my research. Thanks a lot 'Azad Da' for everything you have done for me. Dr. Matthew T. Reiten, being in the neighboring lab for first few years was always somebody whom I looked up for help and he made himself available in spite of his busy schedule for any kind of experimental or theoretical discussion. Several times he and Suchi would come running to my lab to check if I was in tears and tried their best to console me. Thanks Matt and Suchi for being so nice to me. Better days did arrive but only after I moved across the hall.

I owe a lot to Xinchao Lu for all her experimental assistance and training in the cleanroom. She has been a very special member of our group and a complete team player with an absolute unselfish attitude. I would like to thank my colleagues, Dr. Mufei Gong, Dr. Adam Bingham, Dr. Yuguang Zhao, Suchitra Ramani, Prakash Giri, Darpan Pradhan, Utish, Sarika Pokhrel, Jianqiang Gu, Zhen Tian, Sree Harsha and Yongyao Chen for many fruitful discussions and help which I got from them on a very regular basis.

Without my parent's blessings and their best wishes, I would have been nothing. My dad, Mr. Nageshwar Singh and mom Mrs. Nilam Singh had more confidence about my success in life than I actually had and many a times when I was lying low, I got up to work harder and gain strength and success just to live up to their expectations. They could never see me getting weak on any front. I am sure I have made them feel proud.

Several of my friends made my life in Stillwater nice and cheerful by supporting me in several ways and they are Rafiq, Sandeep, Nichlavos, Srinivas, Sumanta, DJ, Linju, Sudeep-Rashmi, Amit Agrawal, Melissa Edwards, Susan Cantrell, Vijay, Rajendra, Divya Pratap and Amit-Bhavana. I am really indebted to all of them.

Finally I would like to thank my committee professors who helped me make this research a success story, Dr. Alan Cheville, Dr. Daqing Piao, Dr. Paul Westhaus, Dr. Bruce Ackerson, Dr. Wicksted, and Dr. G. S. Agarwal. Thank you for being on my committee and guiding me through this research under your watchful eyes.

TABLE OF CONTENTS

Chapter Page

LIST OF FIGURES

Figure Page

LIST OF SYMBOLS

MMs	Metamaterials
SRRs	Split ring resonators
ε_m	Complex dielectric constant of metal
ε_{rm}, ε_{r2}	Real dielectric constant of metals
ε_{im}, ε_{i2}	Imaginary dielectric constant of metals
ω_p	Plasma frequency
ω	Angular frequency, rad/s
N	Free electron density
e	Electric charge of an electron
m_0	Mass of the free electron
h	Plank's constant
$\boldsymbol{E}(\boldsymbol{r},t)$	Electric field
$\boldsymbol{B}(\boldsymbol{r},t)$	Magnetic flux density
$\boldsymbol{E}_z$	Electric field amplitude in z-direction
$\boldsymbol{E}_x$	Electric field amplitude in x-direction
$\boldsymbol{H}_y$	Magnetic field amplitude in y-direction
$\boldsymbol{D}$	Electric flux density
C	Velocity of light in free space, 3×10^8 m/s

ρ	Charge density
J	Current density
$\boldsymbol{P}$	Polarization
$\boldsymbol{M}$	Magnetization
ε_0	Permittivity of free-space, 8.854×10^{-12} F/m
μ_0	Permeability of free-space, $4\pi\times10^{-7}$ H/m
σ_s	Surface charge density
k_x	Wavevector along x-direction
k_z	Wavevector along z-direction
ε_1	Dielectric constant of the dielectric medium
ε_2	Complex dielectric constant of metal
TDS	Time-domain-spectroscopy
SOS	Silicon-on-sapphire
w_2, w_3	THz beam waist
E_{ref}	Reference electric field amplitude
E_{sam}	Sample electric field amplitude
d	Diameter of the aperture
λ	Wavelength in free space
ω_{LC}	Inductive – Capacitive resonance angular frequency of SRRs
ω_{dipole}	Dipole angular resonance frequency of SRRs
ε_r	Real dielectric constant

ε_i	Imaginary dielectric constant
σ_r	Real conductivity
σ_i	Imaginary conductivity
m^*	Effective mass of free carrier
Γ, ω_Γ	Carrier damping rate
UV	Ultra violet
$\varepsilon_\infty, \varepsilon_{Si}$	High frequency dielectric constant
σ_{rm}	Real conductivity of metal
σ_{im}	Imaginary conductivity of metal
$T_{amplitude}$	Amplitude transmission
T_{Power}	Power transmission
δ_m	Skin depth of metal
τ	Carrier collision time
EIT	Electromagnetically induced transparency

CHAPTER I - INTRODUCTION

Light is ultimate means of sending information to and from the interior structure of a material since it packages data in a signal of zero mass and unmatched speed. Light is '*single handed*' when interacting with atoms of conventional materials because only the electric hand is effective in probing the atoms of a material whereas the magnetic hand interaction is too weak. *Metamaterials* are artificial materials with rationally designed properties that allow both field components of light to couple to meta-atoms and thus enable entirely new optical properties and exciting applications with such "*double-handed*" light, the most fascinating property being that of a *negative refractive index* which is the most fundamental characteristic of light propagation in materials. Metamaterials with negative refraction will lead to the development of '*superlens*' capable of imaging objects and fine structures much smaller than the wavelength of light. Other exciting applications will lead to development of optical antennas, nanolithography, nanocircuits and '*metacoatings*' that can make objects *invisible*, giving birth to the technology of electromagnetic *cloak.*

The work presented in this thesis is an experimental study of manipulating terahertz (THz) transmission through subwavelength split ring resonators (SRRs) structured as metal films on silicon substrate. The SRRs mainly have sharp resonance features which are the key to evoking highly dispersive behavior in permittivity as well as permeability. The two prominent resonances are due to the circular current excited in the inductive – capacitive (LC) circuit of the metal split rings and the charged coupled plasmonic oscillations in the metal arms at higher frequency. The work here mainly concentrates on the control of these highly resonant features and studying their in-depth behavior and their potential applications such as biosensing, design of high quality factor devices, developing devices for slow light applications and optical nanoantennas.

1. 1 Electric and magnetic properties of materials

The electric and magnetic properties of materials are determined by two important material parameters, dielectric permittivity and magnetic permeability. Together the permeability and the permittivity determine the response of the material to the electromagnetic radiation. Generally, ε and μ are both positive in ordinary materials. While ε could be negative in some materials (for instance, ε posses negative values below the plasma frequency of metals), no natural materials with negative μ are known. However, for certain structures, which are called left-handed materials (LHMs), both the effective permittivity, ε_{eff} and permeability, μ_{eff} possess negative values. In such materials the index of refraction, n, is less than zero, and therefore, the phase and group velocity of an electromagnetic (EM) wave can propagate in opposite directions such that the direction of propagation is reversed with respect to the direction of energy flow [1]. This phenomenon is called the negative index of refraction and was first theoretically proposed by Veselago in 1968, who also investigated various interesting optical properties of the negative index structures [1].

1. 2 Negative permittivity and permeability

Negative effective permittivity in the microwave frequency range can be achieved by using periodic thin wire media. Dielectric permittivity takes negative values and EM waves cannot propagate inside the medium below the plasma frequency [2]. Electric charge is responsible for a large electric response in dielectric materials. Because of the lack of magnetic charge analogous to electric charge, it is more difficult to obtain a material with negative magnetic permeability. Pendry et al. suggested that a periodic array of artificial structures called SRRs exhibit it negative effective μ for frequencies close to the magnetic resonance frequency [3]. Smith et al. reported the experimental demonstration of LHMs by stacking SRRs and thin rod structures as periodic arrays of one and tow dimensional structured composite metamaterials [4,5]. Theoretical predictions based on calculations and analyses showed that the refractive index is indeed negative, where both ε and μ are simultaneously negative [6]. Experimental observation of negative refraction in LHMs by Shelby et al. [7]. In general, wave propagation in negative index media have also been a controversial subject and have generated an intense debate but over the time extensive experimental studies on negative refraction using different techniques supported the existence of negative refraction [8,9].

1. 3 THz metamaterials

The development of artificially structured metamaterials has led to the realization of phenomena that cannot be obtained with natural materials. This is especially important for the technologically relevant THz (1 THz = 10^{12} Hz) frequency regime because many materials inherently do not respond to THz radiation, and the tools that are necessary to construct devices operating within this range—sources, lenses, switches, modulators and detectors—largely do not exist [10-16]. Considerable efforts are underway to fill this 'THz gap' in view of the useful potential applications of THz radiation. Moderate progress has been made in THz generation and detection; THz quantum cascade lasers are a recent example. However, techniques to control and manipulate THz waves are lagging behind. Here we demonstrate metamaterials capable of efficient real-time control and manipulation of THz radiation. The passive device consists of an array of aluminum, silver or lead electric resonator elements fabricated on a silicon substrate. The design flexibility associated with metamaterials provides a promising approach, from a device perspective, towards filling the THz gap.

1. 4 Organization of this thesis

The report is directed towards probing the characteristics of THz domain metamaterials and optimizing their behavior which would ultimately help the development of sub wavelength THz photonics. Fundamental resonance features of metamaterials can be tuned achieving a huge modulation capacity just by working along the thin film technology. Mastering this art of controlling the propagation of feely propagating THz pulses can lead to development of the much required THz filter and modulators. One of the most important features of THz waves is application in sensing due to many materials having characteristic signatures in this range of frequencies. In this report there is an attempt to design high quality factor metamaterials which can be used for sensing. The optimization technique of Q factors of SRRs has been detailed and also experimentally the sensing capability of the THz is proved.

Chapter 2 is a brief description of the fundamental theories on which the metamaterials work. The dispersion relation for the permittivity and the permeability has been discussed and the condition for which they would become negative which forms the basis for the development of negative index metamaterials.

Chapter 3 shows the experimental setup for time-domain spectroscopy (THz-TDS). Optoelectronic techniques for transmission and detection of pulsed THz radiation are described. A focused beam THz-TDS system is capable of focusing down the THz beam up to a frequency independent beam waist of 3.5 mm.

Chapter 4 is a study of the evolution of the fundamental resonance features of THz metamaterials. It has been shown experimentally as to at what critical thickness of metal split rings does the resonances starts to appear and then increases in strength till it finally saturates at a particular thickness and the transmission remains fixed after that.

Chapter 5 is a demonstration of how the fundamental inductive-capacitive (LC) resonance depends on the permittivity of the metal used for the metamaterial design. The higher conductivity metal shows stronger resonance. The experiment reveals that the conductivity of the metal does not limit the Q factor of the LC resonance but it is the radiation resistance of metal rings with increasing conductivity.

Chapter 6 presents the close interaction study between the SRRs. A comparison is made between SRRs with different symmetry oriented unit cells and different periodicity. Tremendous pulse reshaping is observed for the closely placed SRRs. For one of the super unit cells a Q factor of 18.5 is observed due to a very sharp high frequency resonant dip which has immense potential to be used for sensing applications.

Chapter 7 is the study of pulse propagation through a random media comprising of SRRs whose periodicity changes randomly, though its orientation is kept fixed. We basically observe no change in the fundamental resonance of the SRR but a significant change in the higher order resonances of the random metamaterials.

Chapter 8 is experimental demonstrations of the sensing capability of the SRRs. We see significant shifts in the resonance frequencies of the metamaterial for a dielectric thin film layer of as thin as 100nm. We propose this as a very important effect to sense very small amounts of analytes in the THz frequency domain.

At last, in chapter 9 we attempt to replicate the quantum phenomena of electromagnetically induced transparency (EIT) plasmonic mode coupling in classical THz metamaterial resonators where we describe the limitations of split ring resonators of same size having similar quality factors and Lorentzian coupling between two resonators of same Q factors cannot replicate the real EIT effect.

Finally, chapter 10 summarizes the highlights of this work and its long term implications.

CHAPTER II - FUNDAMENTALS OF METAMATERIALS

2. 1 Definition of metamaterials

Electromagnetic metamaterials (MMs) are broadly defined as artificial effectively homogeneous electromagnetic structures with unusual properties not readily available in nature. An effectively homogeneous structure is a structure whose structural average cell size P is much smaller than the guided wavelength, λ_g . Therefore, this average cell size should be at least smaller than a quarter of wavelength, $P < \lambda_g / 4$. We will refer to the condition $P < \lambda_g / 4$ as the effective homogeneity limit or effective-homogeneity condition1, to ensure that refractive phenomena will dominate over scattering/diffraction phenomena when a wave propagates inside the MM medium. If the condition of effective-homogeneity is satisfied, the structure behaves as a real material in the sense that electromagnetic waves are essentially myopic to the lattice and only probe the average, or effective, macroscopic and well-defined constitutive parameters, which depend on the nature of the unit cell; the structure is thus electromagnetically uniform along the direction of propagation. The constitutive parameters are the permittivity ε and the permeability μ , which are related to the refractive index *n* by

$$n = \pm\sqrt{\varepsilon_r \mu_r}\ , \tag{2-1}$$

where ε_r and μ_r are the relative permittivity and permeability related to the free space permittivity and permeability by $\varepsilon_0 = (\varepsilon / \varepsilon_r) = 8.85 \times 10^{-12}$ and, $\mu_0 = (\mu / \mu_r) = 4\pi \times 10^{-7}$, respectively. In equation (2-1), the sign ± for the double-valued square root function has been a priori admitted for generality. The four possible sign combinations in the pair (ε, μ) are (+, +), (+, −),(−, +), and (−, −), as illustrated in the $\varepsilon - \mu$ diagram of Fig. 2-1. Whereas the first three combinations are well known in conventional materials, the last one [(−, −)], with simultaneously negative permittivity and permeability, corresponds to the new class of LHMs [17].

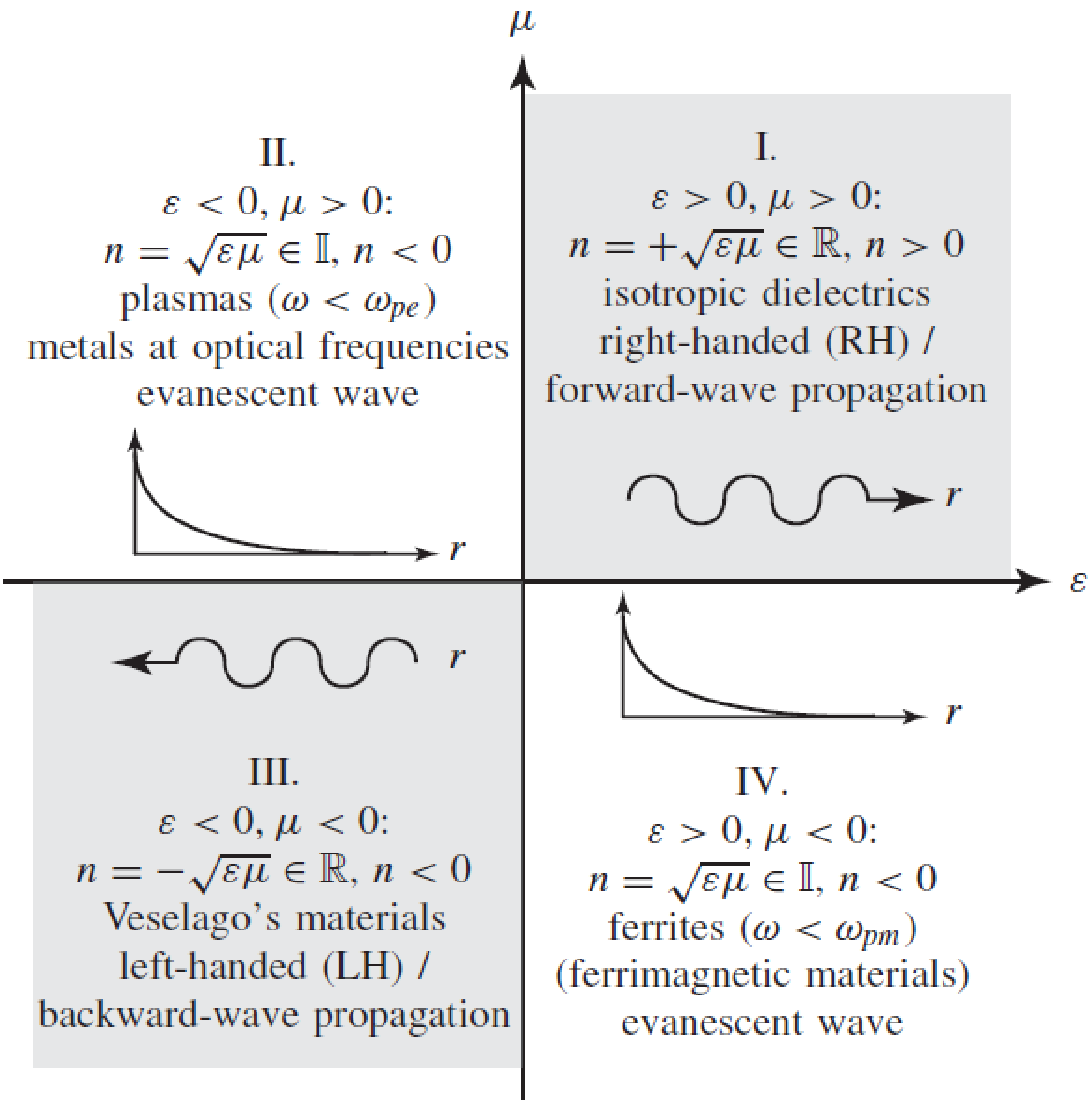

Figure 2-1 Permittivity – Permeability and refractive index diagram [17]

2. 2 Prediction of Veselago

The history of MMs started in 1967 with the visionary speculation on the existence of “substances with simultaneously negative values of ε and μ” (fourth quadrant in Fig. 2-1) by the Russian physicist Viktor Veselago [1]. In his paper, Veselago called these materials as left-handed (LH) to express the fact that they would allow the propagation of electromagnetic waves with the electric field, the magnetic field, and the phase constant vectors building a LH triad, compared with conventional materials where this triad is known to be right-handed. Veselago concluded his paper by discussing potential real (natural) “substances” that could exhibit left-handedness. He suggested that gyrotropic substances possessing plasma and magnetic properties which both ε and μ are tensors (anisotropic structures), could possibly be LH. However, he recognized that we do not know of even a single substance which could be isotropic and have $\mu < 0$, thereby pointing out how difficult it seemed to realize a practical LH structure [17]. No LH material was indeed discovered at that time.

2. 3 Dispersive permittivity and permeability

After Veselago's paper, more than 30 years elapsed until the first LH material was conceived and demonstrated experimentally. This LH material was not a natural substance, as expected by Veselago, but an artificial effectively homogeneous structure which was proposed by Smith and colleagues [4]. This structure was inspired by the pioneering works of Pendry et al [3]. Pendry introduced the plasmonic-type negative-ε/positive-μ and positive-ε/negative-μ structures shown in Fig. 2-2, which can be designed to have their plasmonic frequency in the microwave range. Both of these structures have an average cell size p much smaller than the guided wavelength and are therefore effectively homogeneous structures, or MMs. The negative-ε/positive-μ MM is the metal thin-wire (TW) structure shown in Fig. 2-2(a).

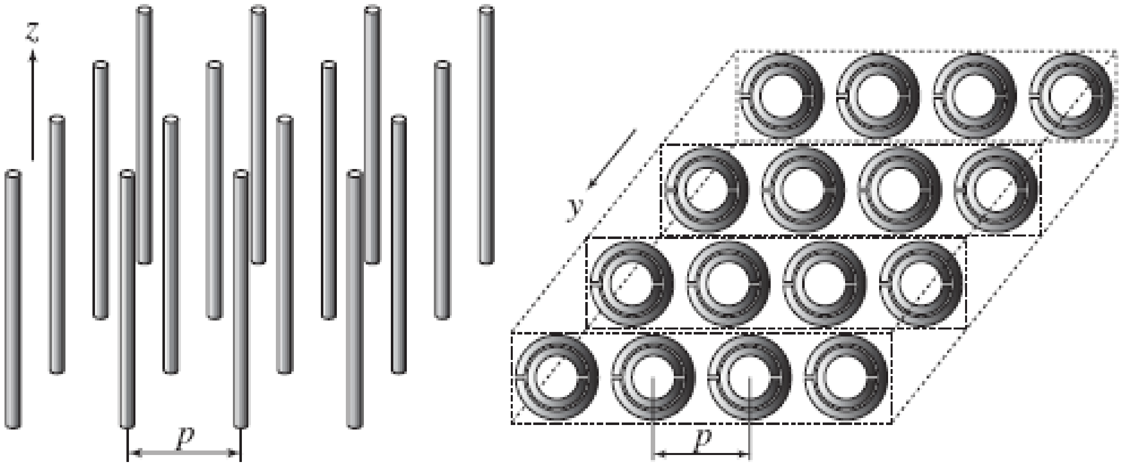

(a) (b)

Figure 2-2 - (a) Thin – wire (TW) structure exhibiting negative - ε / positive – μ if **E** is parallel to z. (b) SRR structure exhibiting positive – ε / negative – μ if **H** is perpendicular to y axis. [3,17]

If the excitation electric field E is parallel to the axis of the wires so as to induce a current along them and generate equivalent electric dipole moments, this MM exhibits a plasmonic-type permittivity frequency function of the form [2]

$$\varepsilon_r(\omega) = 1 - \frac{\omega_{pe}^2}{\omega^2 + j\omega\zeta} \quad ,$$

$$\omega_{pe} = \sqrt{\frac{2\pi c^2}{p^2 \ln(\frac{p}{a})}} \quad , \tag{2-2}$$

$$\zeta = \varepsilon_0 \ (p\omega_{pe} / a)^2 / \pi\sigma \quad ,$$

where ω_{pe} is the tunable electric plasma frequency in gigahertz range and ζ is the damping factor due to metal loss. It is clear from the dispersion relation above that

Re $(\varepsilon_r) < 0$ for $\omega^2 < \omega_{pe}^2 - \zeta^2$ and if $\zeta = 0$ then $(\varepsilon_r) < 0$ for $\omega < \omega_{pe}$ Eq. (2-2) (2-3)

Permeability is simply $\mu = \mu_0$, since no magnetic material is present and no magnetic dipole moment is generated. It should be noted that the wires are assumed to be much longer than wavelength (theoretically infinite), which means that the wires are excited at frequencies situated far below their first resonance. The positive-ε/negative-μ MM is the metal split-ring resonator (SRR) structure shown in Fig. 2-2(b) [3]. If the excitation magnetic field **H** is perpendicular to the plane of the rings so as to induce resonating currents in the loop and generate equivalent magnetic dipole moments, this MM exhibits a plasmonic-type permeability frequency function of the form [3]

$$\mu_r(\omega) = 1 - \frac{F\omega^2}{\omega^2 - \omega_{0m}^2 + j\omega\zeta} \quad ,$$

$$F = \pi\left(\frac{a}{p}\right)^2 \quad , \qquad (2\text{-}4)$$

$$\omega_{0m} = c\sqrt{\frac{3p}{\pi \ln(2wa^3/t)}} \quad ,$$

It should be noted that the SRR structure has a magnetic response despite the fact that it does not include magnetic conducting materials due to the presence of artificial magnetic dipole moments provided by the ring resonators. Eq. (2.4) reveals that a frequency range can exist in which Re $(\mu_r) < 0$ in general $\zeta \neq 0$. In the loss-less case, it appears that ($\zeta \neq 0$), it follows that

$$(\mu_r) < 0 \text{ , for } \quad \omega_{0m} < \omega < \frac{\omega_{0m}}{\sqrt{1-F}} = \omega_{pm} \quad , \qquad (2\text{-}5)$$

where ω_{pm} is called the magnetic plasma frequency.

The equivalent circuit of a SRR is shown in Fig. 2-3 [17]. In the double ring configuration [Fig. 2-3(a)], capacitive coupling and inductive coupling between the larger and smaller rings are modeled by a coupling capacitance C_m and by a transformer (transforming ratio n), respectively. In the single ring conFig.uration [Fig. 2-3(b)], the circuit model is that of the simplest RLC resonator with resonant frequency

$$\omega_0 = \frac{1}{\sqrt{LC}} \quad , \tag{2-6}$$

The double SRR is essentially equivalent to the single SRR if mutual coupling is weak, because the dimensions of the two rings are very close to each other, so that $L_1 \approx L_1 \approx L$ and $C_1 \approx C_1 \approx C$, resulting in a combined resonance frequency close to that of the single SRR with same dimensions but with a larger magnetic moment due to higher current density.

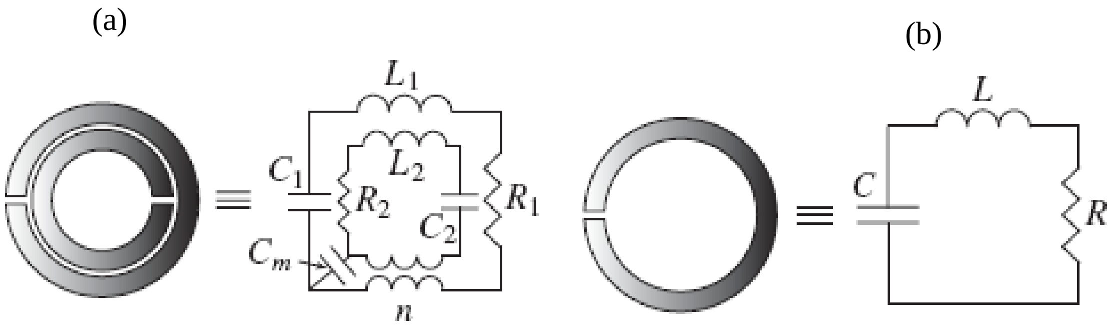

Figure 2-3: Equivalent circuit model of (a) double SRR, (b) single SRR. [17]

In [4], Smith et al. combined the TW and SRR structures of Pendry into the composite structure which represented the first experimental LH MM prototype. The main arguments in [4] consisted that of designing a TW structure and a SRR structure with overlapping frequency ranges of negative permittivity and permeability; combining the two structures into a composite TW-SRR structure, and launching an electromagnetic wave $e^{-j\beta r}$ through the structure and concluding from a fact that a pass band (or maximum transmission coefficient, experimentally) appears in the frequency range of interest proves that the constitutive parameters are simultaneously negative in this range on the basis of the fact that $\beta = nk_0 = \pm\sqrt{\mu_r \varepsilon_r}$ has to be real in a pass band.

CHAPTER III

EXPERIMENTAL SET UP FOR TERAHERTZ TIME DOMAIN SPECTROSCOPY (THz-TDS)

3. 1 THz time-domain spectroscopy

The THz-TDS is a spectroscopic technique where a special generation and detection scheme is used to probe the material properties with short pulses of THz radiation [18]. The generation and detection scheme is sensitive to the sample material's effect on both the amplitude and phase of the THz pulses. This particular spectroscopy technique gives extra phase information compared to the other conventional spectroscopy methods like Fourier transform spectroscopy which is sensitive only to the amplitude. The amplitude and phase are directly related to the absorption coefficient and index of refraction of the sample and thus the complex valued permittivity of the sample can be obtained without having to carry out the Kramers- Kronig analysis. The THz-TDS has several other advantages like many materials have unique spectral behavior in the THz frequency range. There are materials which are transparent to THz pulses. THz radiation is harmless for the biological cells and tissues due to its non ionizing nature.

3. 2 Broadband 8F confocal THz-TDS set up.

The transmission lines of the transmitter chip are biased under a dc voltage of 70 Volts. Mode-locked Ti:sapphire laser with pulse width of 26-fs, repetition rate of 100 MHz and a central wavelength of 800 nm is focused on the inside edge of the positively biased transmitter transmission line which generates electron-hole pairs and the ballistic acceleration of these electrons generates a single-cycle THz electromagnetic radiation [18,19]. The high-resistivity silicon lens attached on the back side of the transmitter collimates the transmitted THz radiation into Gaussian beam with 1/e-amplitude waist of diameter 6 mm. In a conventional 4F THz-TDS system, the radiated THz electromagnetic pulses are collimated by another parabolic mirror and are focused to the antenna of the receiver chip with another silicon lens similar to the transmitter side. The receiver antenna, photoconductively switched by another femtosecond optical pulse from the same Ti:Sapphire laser, is sensitive to the polarization of the THz radiation. The receiver is connected to a lock-in amplifier through a low-noise current amplifier. When gated, the receiver generates a dc current which is proportional to the instantaneous electric fields of the received THz electromagnetic wave. By changing the relative time delay between the optical gated pulse and the detected THz pulse the entire pulse shape of the THz radiation can be mapped out as a function of the relative time delay which includes both amplitude and phase information.

3. 3 8-F THz-TDS system

Standard THz-TDS system is modified in order to measure samples with comparatively smaller dimensions by introducing an additional pair of parabolic mirrors in the middle of two major parabolic mirrors as shown in Fig. 3-1. The parabolic mirrors are arranged in 8-F confocal geometry which provides excellent beam coupling between the transmitter and receiver [19]. The inner parabolic mirrors M_3 and M_4 are identical with a focal length of 50 mm. The Gaussian beam of THz pulses is focused to a frequency-independent beam waist of diameter 3.5 mm at the center between M_3 and M_4 mirrors. The transmitted THz reference pulse and the corresponding frequency spectrum are shown in Fig.. 3-2.Pico-second pulses of 4.0 THz usable bandwidth extending from 0.1 to 4.0 THz is measured. To eliminate the effects of the water vapor the entire THz system is enclosed in a box and purged with dry air during data acquisition.

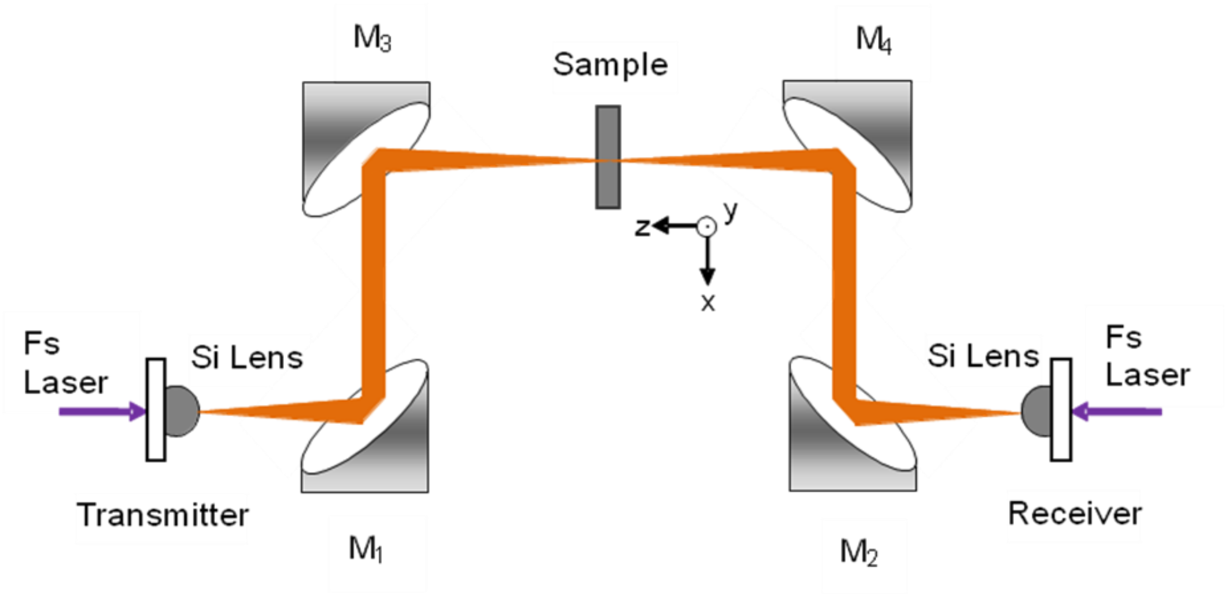

Figure 3-1 - Schematic diagram of modified THz-TDS setup with an 8-F confocal geometry. Smallest beam waist is obtained between mirrors M3 and M4 [18,19].

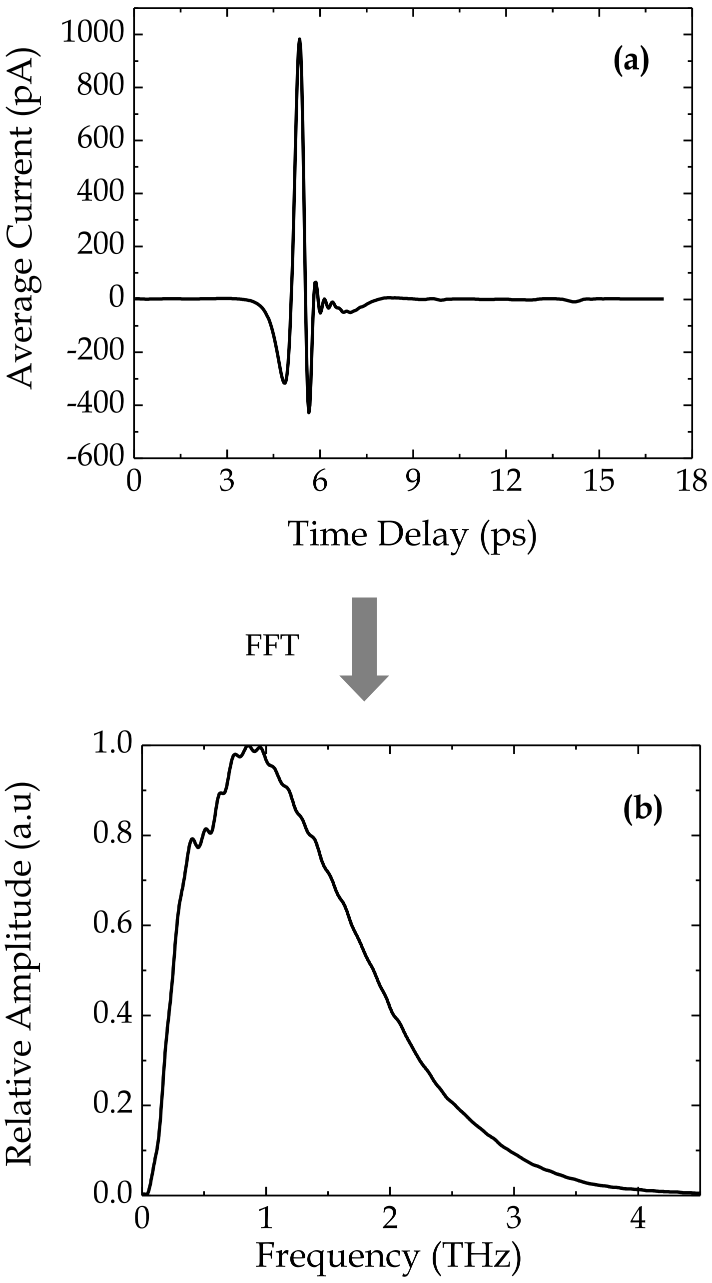

Figure 3-2 - (a) Measured THz reference pulse of the system through air, (b) corresponding frequency spectrum of the reference pulse [14].

CHAPTER IV

EVOLUTION OF RESONANCES IN OPTICALLY THIN METAMATERIALS

4. 1 Introduction

Plenty of research has been focused on the resonances of the SRRs. It has also been found that SRRs exhibits a strong electric resonance at normal wave incidence at the same frequency as the magnetic resonance [16] and is very often called as electrically excited magnetic resonance (EEMR). This particular resonance is extremely important to characterize the behavior of metamaterials since it is difficult to do the transmission measurements for the in plane incidence in the THz and the optical domain and get the actual magnetic resonance. Therefore, in this chapter we probe into the evolution of the EEMR resonance and the higher frequency dipole resonance by varying the thickness of the metal layers forming the split rings deposited on silicon substrate on the sub skin depth scales.

4. 2 Equivalent RLC circuit model of a split ring resonator

The behavior of the main Lorentzian resonance in SRRs is well-known and follows the form of a series RLC circuit [20]. The inductances, L, in the circuit results from current circulating around the SRR perimeter, while the capacitance, *C*, is due to charge accumulation at the gaps. For double SRRs there is an additional capacitive contribution between the two rings. A higher circulating current should result in a stronger resonance. The resistance of the metallic SRRs is directly correlated to the circulating current, and plays a very important role in making these subwavelength structures highly resonant. The induced voltage equation in an RLC circuit can be described as

$$V = L\frac{dI}{dt} + IR + \frac{Q}{C} \quad , \tag{4-1}$$

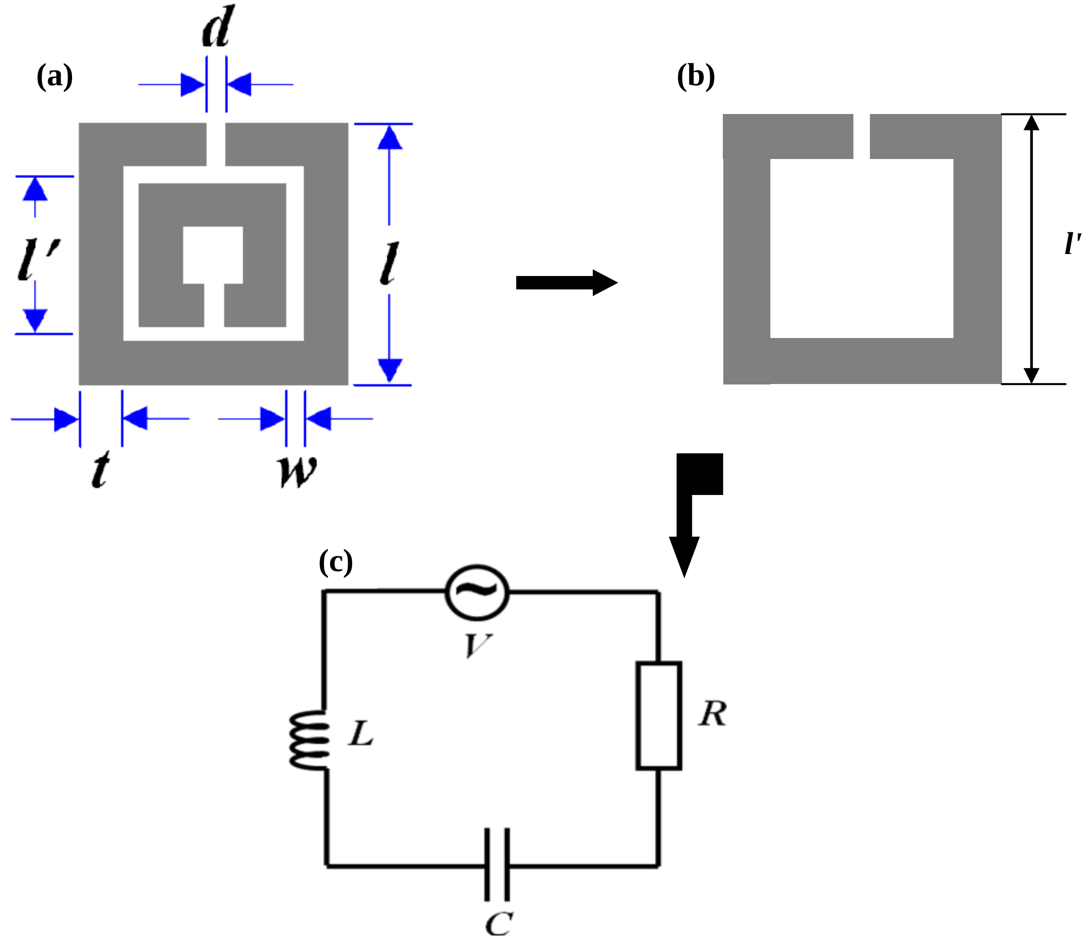

Figure 4-1 – (a) Double SRR with specific dimensions of d = 2 µm, l = 36 µm, w = 3 µm, t = 6 µm, l' = 21 µm and periodicity, P = 50 µm. (b) Equivalent single SRR of double SRR shown in (a). (c) Equivalent RLC circuit.

4. 3 Depth of penetration and internal impedance of metals.

From Maxwell's equations it is seen that the magnitude of the fields and current decrease exponentially with penetration into the conductor and the depth at which they decrease to 1/e of their values at the surface is called depth of penetration or skin depth, denoted as δ. The phases of the current and fields lag behind their surface values by 'x/δ' radians at depth 'x' into the conductor. The skin depth for metals is calculated using the expression

$$\delta = \sqrt{\frac{1}{\pi f \mu_0 \sigma_{dc}}} \quad , \tag{4-2}$$

where f is the frequency at which the skin depth is defined, μ_0 is the vacuum permeability, and σ_{dc} is the d.c. conductivity of metal [21]. The calculated skin depths for Pb, at the LC resonance frequency 0.5 THz is 336 nm at room temperature.

The decay of fields into a good conductor or superconductor may be looked at as the attenuation of a plane wave as it propagates into the conductor or from the point of view that induced fields from the time – varying currents tend to counter the applied fields. The latter point of view is especially applicable to circuits, in which case we think of the field at the surface as the applied field. Currents concentrate near this surface and the ratio of the surface electric field to current flow gives an internal impedance for use in circuit problems. Internal impedance is the contribution to impedance from the fields penetrating the conductor. The total current flowing past a unit width on the surface of the plane conductor is calculated by integrating the current density, from the surface to the infinite depth.

$$J_{sz} = \int_0^\infty J_z dx = \int_0^\infty J_0 e^{-(1+j)(x/\delta)} dx = \frac{J_0\delta}{1+j} \quad . \tag{4-3}$$

The electric field at the surface is related to the current density at the surface by

$$E_{z0} = \frac{J_0}{\sigma} \quad .$$

Internal impedance for a unit length and unit width is defined as [21]

$$Z_s = \frac{E_{z0}}{J_{sz}} = \frac{1+j}{\sigma\delta} = R_s + j\omega L_i \quad ,$$

$$R_s = \frac{1}{\sigma\delta} = \sqrt{\frac{\pi f \mu}{\sigma}} \quad , \tag{4-4}$$

$$\omega L_i = \frac{1}{\sigma\delta} = R_s \quad .$$

The above equations shows that the skin-effect resistance of the semi-infinite plane conductor is the same as the dc resistance of a plane conductor of depth δ . The resistance R_s of the plane conductor for a unit length and unit width is called the surface resistivity.

4. 4 Effective resistance model of SRRs

Ohmic losses are introduced in the equivalent model of SRRs by means of the effective resistance, of the SRR. This effective resistance is obtained by using the equivalent ring model for the current distribution on the SRR. The resistance can be approximated

$$R_{eff} = \frac{4l'}{th\sigma} \qquad \text{for} \qquad h < 2\delta \quad ,$$

and (4-5)

$$R_{eff} = \frac{2l'}{t\delta\sigma} \qquad \text{for} \qquad h \geq 2\delta \quad ,$$

where l' is the average side length of the SRRs, t is the width of the metal lines, and h and σ being the thickness and conductivity of the SRR film, respectively [20].

4. 5 Sample Processing

Here, Lead (Pb) is chosen as the constituent metal for optically thin SRRs because of its large value of skin depth. This allows for a remarkable dynamic range in characterizing the resonance evolution with various sub-skin-depth thicknesses [19, 22]. In addition, Pb behaves as a good conductor at THz frequencies with a high complex conductivity $\sigma = 4.5\times10^6 + i4.9\times10^4\,\Omega^{-1}\mathrm{m}^{-1}$ at 0.5 THz which facilitates establishing the well-defined LC and dipole resonances in the SRR metamaterials.

Pb split ring arrays with various thicknesses ranging from 34 to 672 nm were prepared. The thin metallic film of Pb is deposited on a 0.64-mm-thick p-type silicon wafer with a resistivity of $\rho = 20\ \Omega$-cm. Conventional photolithographic processes are used to form a 50 µm × 50 µm SRR arrays. During metallization, the thickness of the metal films controlled with high precisions to get the right thickness. The thickness of the metal deposited on deposition monitor is different than that of the substrate because they have different distances and different angles. A correction factor, called tooling factor, should be obtained for any particular position of the substrate and the monitor to get the accurate film thickness on the substrate. A water cooled deposition monitor FMT6 has a thickness resolution of 0.1 nm. Deposited metal on the monitor's quartz crystal changes its frequency. The change in the frequency and the density of the deposited metal is used to calculate the thickness of the film. To find the tooling factor, three different-thickness-samples were prepared for a particular position of the substrate with respect to the monitor. We recorded the corresponding thicknesses showed in the monitor. The chamber pressure was 2.5×10^{-5} MB and was not allowed to exceed 3.0×10^{-5} MB during the deposition. We adjusted the current to get a deposition rate 1-2 nm/s. After deposition the film thicknesses were measured by atomic microscopy (AFM) system which showed that the real thickness of the metal films on the substrate was approximately 60% of the thickness observed on the monitor [19]. The thickness of the film is given by

$$d = \frac{Me}{\pi r^2}\cos\phi\cos\theta \quad , \qquad (4\text{-}6)$$

where, Me molecular weight, r is the distance of the substrate from source, ϕ is the angular position of the substrate, and θ is the angle between the substrate normal and the direction of flux. The measured value of r, ϕ, and θ for substrate were 210 mm, 23°, and 7°; and for monitor those were 160 mm, 21°, and 25°. If we consider the sticking coefficient of monitor crystal and silicon substrate are same then the calculated tooling factor was ~62%, which was fairly close to the measured value. To find the real thickness of the substrate film, the monitor thickness was always scaled by 60%. For every metallization, the samples were carefully placed in the same position. For thin film the deposition rate was ~ 0.2-0.3 nm and for the thick film was 1.0-2.0 nm. Density Pb is maintained at 11.34 g/cc. One of the fabricated Pb double rings SRR sample is shown in Fig. 4-2.

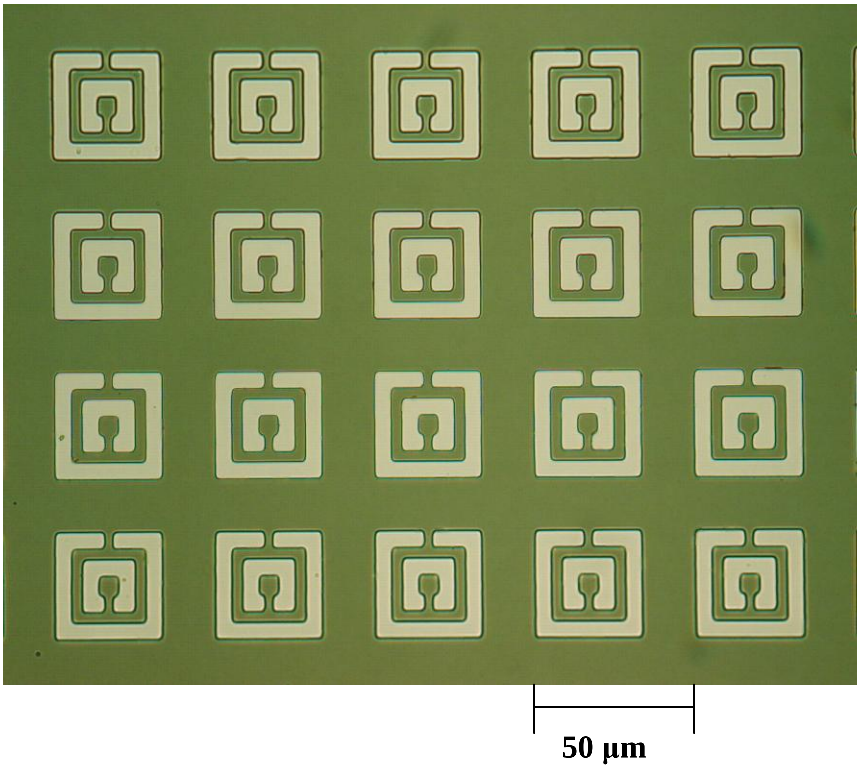

Figure 4-2 – Image of SRRs fabricated by conventional photolithography and 170 nm of Pb metal film is evaporated in a vacuum chamber for the split rings to be formed on silicon substrate.

4.6 Experimental results

A set of Pb SRR arrays of various thicknesses, ranging from 0.1δ to 1.7δ (571 nm) is fabricated by conventional photolithography processing on a silicon substrate (0.64-mm-thick, p-type resistivity 20 Ω cm). The Figure 4-1 shows a diagram of the double SRR with a minimum feature $d = 2$ μm in the splits of the rings and other dimensions of $w = 3$ μm, $t = 6$ μm, $l = 36$ μm, and a lattice constant $P = 50$ μm. Each SRR array has a 20 mm × 20 mm clear aperture. The SRR metamaterials are characterized by THz-TDS in a broadband, photoconductive switch based system that consists of four parabolic mirrors in an 8-F confocal geometry as discussed in chapter 3. The orientation of SRRs is such that the THz electric field is perpendicular to the splits in the rings. The SRR array is placed at the waist of the 3.5-mm-diameter, frequency-independent focused beam, and the THz radiation penetrates the SRRs at normal incidence.

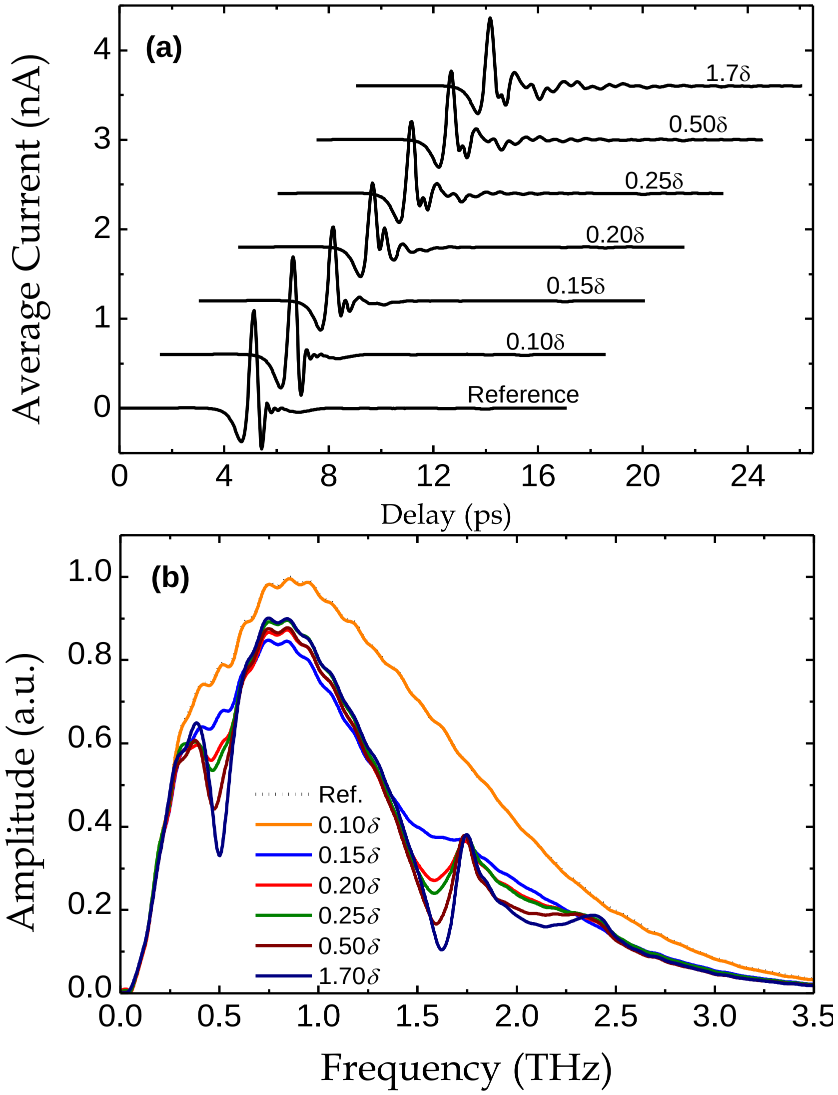

Figure 4-3 - (a) Transmitted THz pulses through the reference and Pb SRR metamaterials of different thicknesses. (b) Corresponding Fourier transformed spectra that illustrate the evolution of the resonances. The E-field of the THz pulses is perpendicular to the SRR gaps.

Figure 4-3 (a) shows an evolution of the pulses transmitted through a reference and the SRR arrays of various thicknesses, and the corresponding Fourier transformed amplitude spectra are illustrated in Fig.. 4-3 (b). The reference is a blank silicon slab identical to the SRR substrate. The transmitted THz pulses as well as the spectrum for the 0.1δ thick SRRs appear nearly identical to the reference, showing that such a thin SRR is almost transparent to the incident THz pulses. However, when the SRR thickness is increased to 0.15δ, a 35% peak-to-peak attenuation and a reshaping of the pulse in the time domain is clearly observed. A further 25% peak-to-peak attenuation also occurs by increasing the thickness to 0.2δ. Also, an adjoining feature along with the main pulse is revealed, which becomes most distinguished for the 0.2δ thick SRRs and then gradually disappears with thicker Pb films. In the frequency domain, three distinct resonances are developed as transmission dips with increasing SRR thickness. They are the LC resonance, ω_{LC} at 0.5 THz, the electric dipole resonance, ω_0 at 1.6 THz, and a weaker electric quadrupole resonance near 2.0 THz. The LC resonance is due to inductive currents circulating around the ring perimeter in conjunction with capacitive charge accumulation at the ring gaps. In contrast, the dipole and quadrupole resonances are due to antenna-like couplings between the two and four SRR sides parallel to the incident electric-field, respectively [16]. The signature of the LC resonance begins to show up with the 0.15δ thick SRRs, while it sharpens to a greater extent with the 0.2δ thick SRRs. Thus, a critical thickness exists near 0.15δ that is required to excite the LC resonance for the Pb film. A further reshaping of the time-domain pulses and the corresponding strengthening of resonances in the spectra occur for SRRs with higher thicknesses.

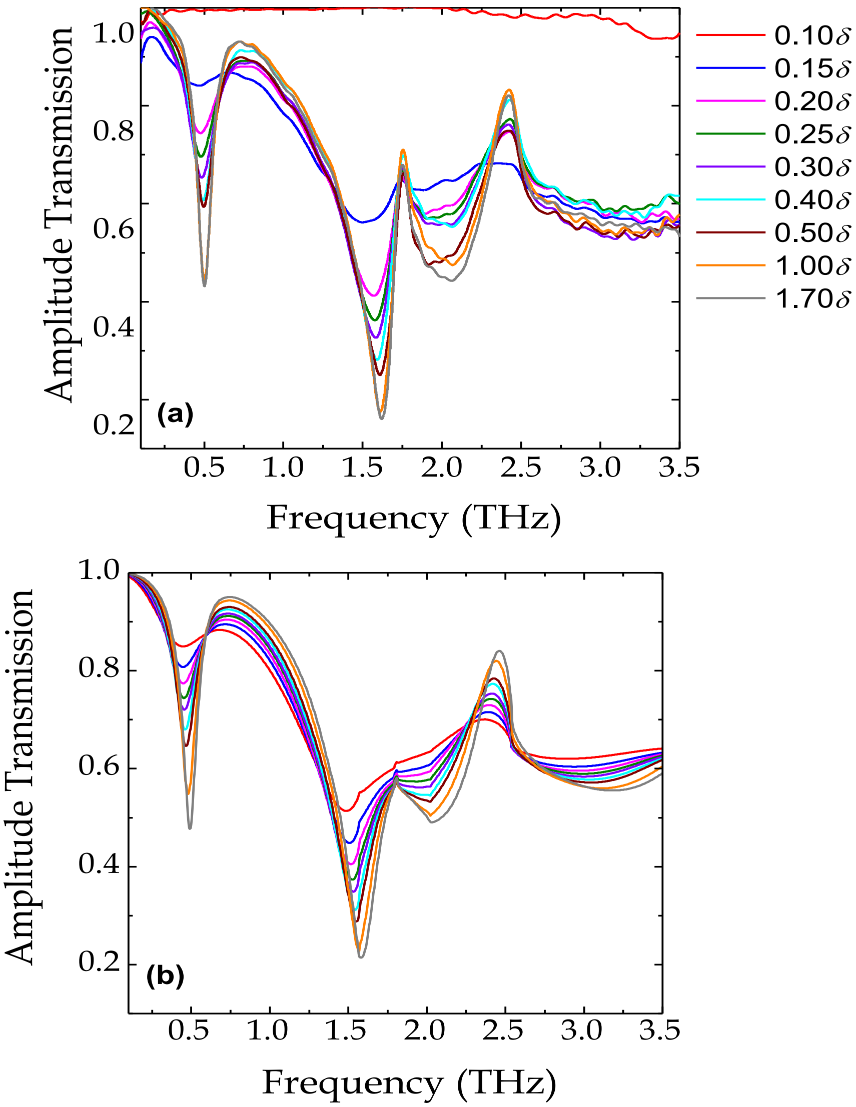

Figure 4-4 - (a) Frequency dependent amplitude transmission of the SRR metamaterials with various thicknesses of Pb film. (b) Corresponding simulation result by CST Microwave Studio.

4. 7 Discussion and analysis

The behavior of the main Lorentzian resonance in SRRs is well-known and follows the form of a series RLC circuit. The inductances, L, in the circuit results from current circulating around the SRR perimeter, while the capacitance, *C*, is due to charge accumulation at the gaps. For double SRRs there is an additional capacitive contribution between the two rings. A higher circulating current should result in a stronger resonance. The resistance of the metallic SRRs is directly correlated to the circulating current, and plays a very important role in making these subwavelength structures highly resonant [3,12,20]. The decrease in effective resistance *R* of the SRRs is mainly responsible for the enhanced LC resonance with increasing sub-skin-depth thickness. The effective resistance of the SRRs can be estimated by the equivalent ring model for current distribution [20]. For the square double SRRs, the effective resistance is approximately given as by Eq. (4-5). The calculated thickness dependent effective resistance of the Pb SRR is shown in Fig. 4-5(b). The effective resistance follows a $1/h$ functional form that is similar to the behavior of the resonance transmission minimum, shown in Fig. 4-5(a). In using RLC circuits to model wave propagation through metamaterials the functional dependence of the transmission is dependent on the overall surface impedance, which incorporates several effects in addition to ring resistance R, such as substrate permittivity, ring density, and other factors. Therefore, the evolution of the transmission minimum is not expected to exactly follow a $1/h$ form. Also, the aforementioned formula used for calculating R assumes that the metal conductivity is thickness independent, which is not necessarily true [23,24]. Nevertheless, the data indicate that the sub-skin-depth metals are basically acting as distributed resistors impeding current flow but causing few other changes in the resonant behavior of the ring. The slight resonance shifts that develop with increasing metal thickness do not necessarily indicate an evolution in the capacitance or inductance of the SRRs, but rather may be the result of coupling between resonant modes of the individual rings along with the individual resonances, causing some reshaping.

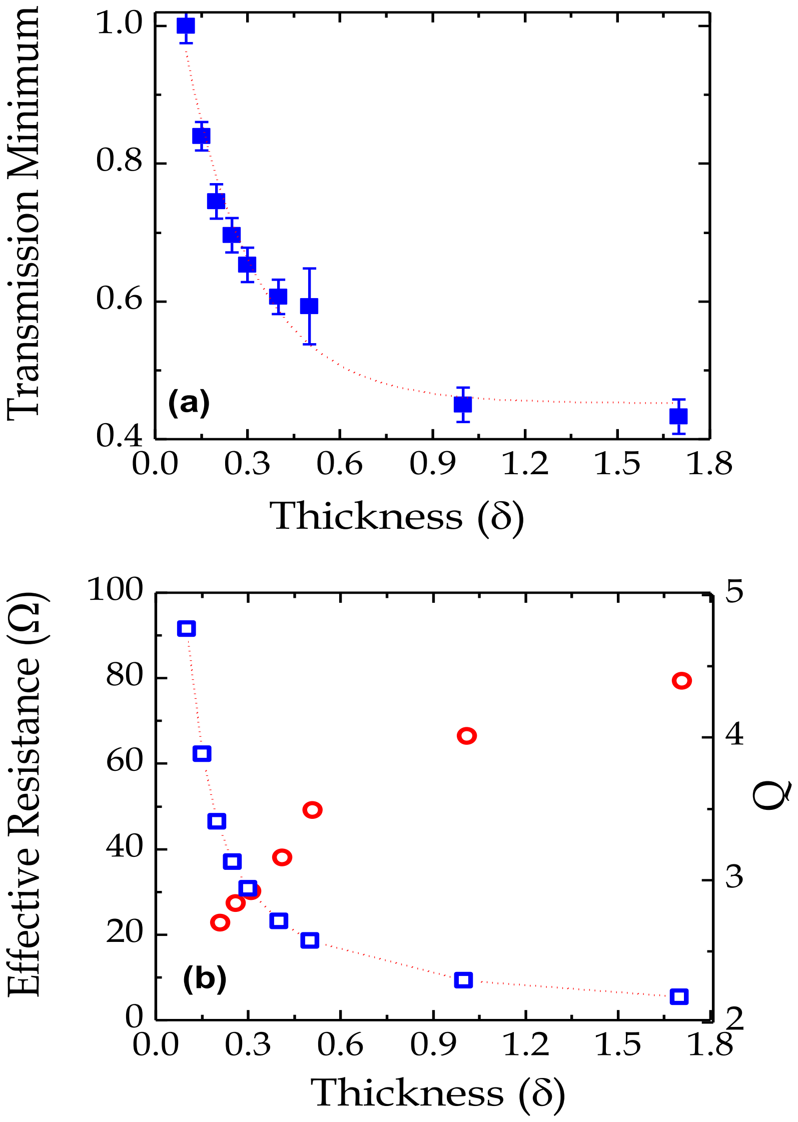

Figure 4-5 - (a) Transmission minimum at the LC resonance as a function of the SRR thickness in skin depth. (b) Calculated effective resistance of the Pb SRR metamaterials

Another related effect observed in the data is the thickness dependent behavior of the quality (Q) factor of the LC resonance. The Q is a measure of the sharpness of a resonance as defined by the central resonance frequency divided by the measured 3dB power bandwidth, $f_0/\Delta f_{3dB}$. As shown in Fig. 4-5(b), the measured Q of the SRR LC resonance is improved with increasing metal thickness. It is worth noting, although from the data we observe that the dipole mode at 1.6 THz begins to develop just as it did at 0.5 THz, the 0.15 skin depth criterion for the LC resonance is not necessarily applicable across the spectrum. This is because the higher-order modes do not share the same current profiles as the LC mode. In fact, dipole currents are largely restricted to the side arms parallel to the THz electric field, whereas LC currents oscillate around the entirety of the ring. In other words, one cannot assume a constant current distribution throughout the ring for anything but the LC resonance [20]. Thus the resistance formula may not be valid for higher-order resonances. For this reason we need not expect damping behavior to be the same for LC and higher resonances.

Simulations using CST Microwave Studio were carried out to model the sub-skin-depth resonators [26]. Modeling the Pb films as lossy metals did not produce results that agreed with the experiments. This is because Microwave Studio does not solve Maxwell’s equations inside metallic geometries, instead setting up Leontovich boundary conditions on the metal surface. As a result, metallic inclusions of any thickness appear thicker than a skin depth. Therefore, the software was forced to treat the Pb layers as dielectrics having very high permittivity and conductivity (σ = 4.5 × 10^6 $\Omega^{-1}m^{-1}$, ε = –1800). As shown in Fig. 4-4(b), this resulted in good agreement with the experimental data capturing most of the measured behavior, including the slight frequency shifting of the resonance with increasing metal thickness. The simulations elucidate the nature of many of the features in the data, such as the onset of various higher-order modes (1.8 THz, 2.54 THz), but also reveal additional information. For example, the simulated transmission minimums follow a very uniform decrease with increasing metal thickness, more so than in the measurements. This reveals a possible experimental variation in the Pb conductivity with thickness or a tolerance in the deposited thickness. Such variations are not altogether unexpected in sub skin-depth layers of metals due to non-uniform or non-crystalline growth. Further studies are also being pursued to discover the nature of unique features such as the one at 0.6 THz in which the thickness of the metal seems to have no effect on transmission.

4. 7 Summary of Results

We have experimentally demonstrated optically thin metamaterials resonating in the THz regime. The thickness dependent resonance evolution characterized by THz-TDS has shown that remarkable electromagnetic resonances can be developed in planar metamaterials of sub-skin-depth thicknesses. In particular, nearly 70% of the maximum resonance amplitude was achieved in the half-skin-depth thick Pb SRR array. Similar resonance behavior was also observed in optically thin metamaterials made from Ag and

Al. The sub-skin-depth approach enables the control and modification of resonance magnitude of a fixed metamaterial design and will benefit applications in integrated subwavelength THz components.

CHAPTER V

EFFECT OF METAL PERMITTIVITY ON THE RESONANCES OF METAMATERIALS

5. 1 Introduction

In this chapter we investigate the effect of metal permittivity on resonant transmission of metamaterials by THz-TDS. Our experimental results on double SRRs made from different metals confirm the recent numerical simulations [27] that metamaterials exhibit permittivity dependent resonant properties. The measured inductive-capacitive resonance is found to strengthen with a higher ratio of the real to the imaginary parts of metal permittivity and this remains consistent at various metal thicknesses. Furthermore, we found that metamaterials made even from a generally poor metal become highly resonant due to a drastic increase in the value of the permittivity at THz frequencies.

Most metamaterials utilize SRRs to achieve a desired response. The electric permittivity ($\varepsilon_m = \varepsilon_{rm} + i\varepsilon_{im}$) of metal SRRs is an important factor that is closely associated with the establishment of LH resonance in metamaterials [27]. In typical SRRs, the fundamental resonance is inductive-capacitive (LC) in nature, where circulating current flow in the metallic loops creates an inductive effect and charge accumulation at ring gaps provides capacitance. The complex permittivity of the metal, ε_m used to fabricate the SRRs plays a very important role in making the structure highly resonant. Although the exact values of ε_m were not known, a recent numerical study investigating the resonance properties of microwave SRR-based metamaterials verified this dependence on ε_m . By fixing the real part of permittivity to $\varepsilon_{rm} = 1$, and increasing the magnitude of the imaginary permittivity, the resonance gap of SRRs was found to become narrower and the left handed effect was further enhanced.

At THz frequencies, the values of metal permittivity are several orders of magnitude higher than those at optical frequencies, but obviously lower than those in the gigahertz region. No study was performed to see how the electric permittivity of metals influences the resonant behavior of metamaterials in the THz regime. In this chapter, we present a THz-TDS study of the effect of metal permittivity on transmission properties of double SRR metamaterials. An LC resonance centered at 0.5 THz is well pronounced in metamaterials made from various metals, including so-called good metals, Ag and Al, as well as a generally poor metal, Pb. Properties, such as the resonance transmission amplitude and linewidth are shown to exhibit dependence on the electric permittivity of the constituent metals. In particular, the resonant transmission dip is enhanced in correspondence with an increase in the imaginary part of the permittivity, ε_{im} , or an increase in the ratio of the real to the imaginary permittivity, $-\varepsilon_{rm}/\varepsilon_{im}$, showing consistency with recent numerical predictions at microwave frequencies. A CST Microwave Studio simulation is also carried out to supplement the THz-TDS results.

5. 2 The Drude Model of free electrons in metals

The simple Drude model treats the free carriers in a metal as classical point charges subject to random collisions for which the collision damping is independent of the carrier velocity. According to the model, the frequency-dependent complex dielectric constant, $\varepsilon(\omega)$ [32].

$$\varepsilon(\omega) = \varepsilon_r(\omega) + i\varepsilon_i\left(\omega\right) = \varepsilon_\infty + \frac{i\sigma\left(\omega\right)}{\omega\varepsilon_0} = \varepsilon_\infty - \frac{\omega_p^2}{\omega^2 + i\omega\Gamma} \quad , \qquad (5\text{-}1)$$

where Drude conductivity is given as

$$\sigma\left(\omega\right) = \sigma_r\left(\omega\right) + i\sigma_i\left(\omega\right) = \frac{\sigma_{dc} i\Gamma}{\omega + i\Gamma} = \frac{i\varepsilon_0\omega_p^2}{\omega + i\Gamma} \quad , \qquad (5\text{-}2)$$

where ε_∞ dielectric contribution from bound electrons, ε_r and ε_i are the real and imaginary part of the dielectric constants, ω is the angular frequency, ε_0 is free space dielectric, and $\sigma(\omega)$ is the complex conductivity, σ_r and σ_i are the real and imaginary conductivity; dc conductivity, $\sigma_{dc} = e\mu N$, μ being the electron mobility, Γ is the carrier damping rate; and ω_p is the plasma frequency. The plasma frequency ω_p is defined as $\omega_p = \sqrt{Ne^2/\varepsilon_0 m^*}$; where N is the carrier density, e is the charge of the electron, ε_0 is free space dielectric, and m^* is the effective mass of the electron. The effective electron mass of silicon is 0.26m_0, where m_0 is the mass of free electron. The real and imaginary parts of the complex conductivity are given by,

$$\begin{aligned} \sigma_r(\omega) &= \frac{\varepsilon_0 \omega_p^2 \Gamma}{\omega^2 + \Gamma^2} \quad , \\ \sigma_i(\omega) &= \frac{\varepsilon_0 \omega_p^2 \omega}{\omega^2 + \Gamma^2} \quad , \end{aligned} \tag{5-3}$$

The real and imaginary parts of the complex dielectric constants are given by,

$$\begin{aligned} \varepsilon_{rm} &= \varepsilon_\infty - \frac{\omega_p^2}{\omega^2 + \Gamma^2} \quad , \\ \varepsilon_{im} &= \frac{\omega_p^2 \Gamma}{\omega(\omega^2 + \Gamma^2)} \quad , \end{aligned} \tag{5-4}$$

For microwave and THz frequencies $\frac{\omega}{\Gamma} << 1$ and the metal permittivity can be approximated as [28]

$$\varepsilon_m \approx -\frac{\sigma_{dc}}{\varepsilon_0 \Gamma} + \frac{i\sigma_{dc}}{\varepsilon_0 \omega} \quad , \tag{5-5}$$

The resulting dielectric constant for conducting metals has a negative constant real part and a much larger frequency-dependent imaginary part.

5. 3 Sample Processing

The SRR samples were fabricated on a 0.64-mm-thick P-type silicon wafer which had a resistivity of $\rho = 20\ \Omega$ cm. Then a positive photoresist SR 4000 was applied and spun at 3000 rpm for another 30 second. At this speed the thickness of the photoresist layer was approximately 4 µm after which followed 15 minutes of soft bake at 100 degrees in the baking unit. The wafer was then exposed with a contact mode mask aligner using UV light (λ = 436 nm) while under the mask. The sample was developed using immersion methods in a full concentration RD6 developer. For metallization three different metals were chosen, those are, silver, aluminum, and lead. Metal thicknesses for the metallization were carefully chosen to be equal to the skin depth at 0.5 THz LC resonance frequency. An 84-nm-thick metal layer was chosen for silver, 116nm for aluminum array and a 336-nm-thick metal layer was chosen for lead sample as one skin depth thickness. So, totally nine sets of SRR structures were fabricated, three with half skin depth metal films, three with one skin depth and another three two skin depth of Ag, Al and Pb metals. Metal films were then thermally evaporated on the patterned photoresist using a thermal evaporator (BOC Edward 306) at vacuum pressure of 2.5×10^{-5} mB and a deposition rate of 3 nm. After the lift-off step SRRs array of with periodicity of 50 µm was formed.

5. 4 Experimental Measurement

Figure 5-1 shows the measured amplitude transmission of the SRR metamaterials made from different metals near the LC resonance. The transmission is extracted from the ratio of the Fourier-transformed amplitude spectra of the samples to the reference. The reference is a blank silicon slab identical to the SRR substrate. When the planar SRRs are 0.5δ thick, as shown in Fig. 5-1(a), a well-defined LC resonance develops at 0.5 THz. The difference in resonance strength for different metals is clearly seen, with Ag SRRs featuring the deepest resonant transmission of 53.9%, while Al and Pb SRRs are limited at 60.2% and 64.4%, respectively. The resonant behavior of the SRRs is further compared by using metals with different thicknesses. As shown in Fig.s. 5-1(b) and 5-1(c), with increasing metal thickness to 1.0δ and 2.0δ, the resonance is further strengthened for all metals. The Ag SRRs consistently reveal the strongest resonance, having a transmission dip reduced to 18.5% at a thickness of 2.0δ. Comparatively, for the 2.0δ thick Al and Pb samples, the transmissions are 30.2% and 43.1%, respectively. The measured transmission amplitudes at the LC resonance minima are plotted in Fig.. 5-2(a) as a function of metal thickness. It is worth noting when the metal thickness is varied from 1.0δ to 2.0δ, the LC transmission for the Pb metamaterials is nearly saturated, while it is continuously strengthened for the Ag SRRs.

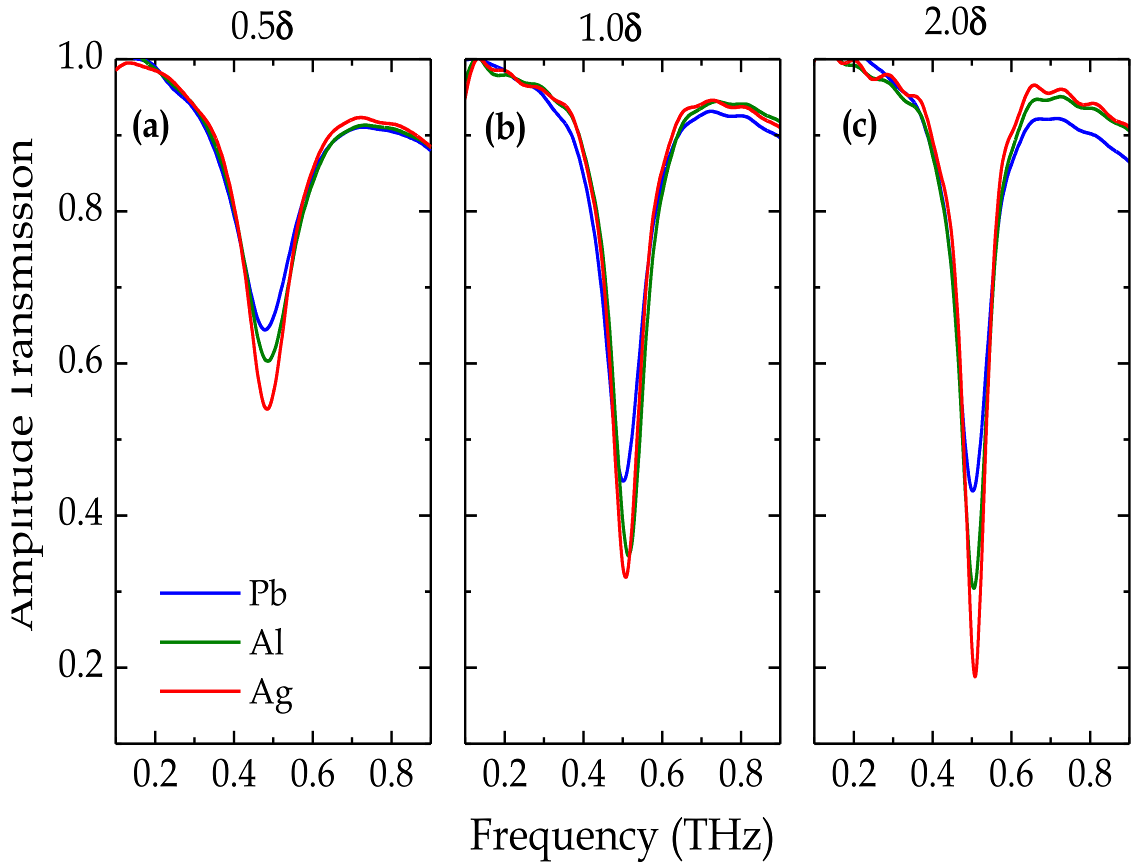

Figure 5-1 - Measured frequency dependent amplitude transmission of planar double SRR metamaterials made from Pb, Al, and Ag with various film thicknesses: (a) 0.5δ, (b) 1.0δ, and (c) 2.0δ, near the LC resonance.

5. 5 Analysis and comparison with theory

At 0.5 THz, the complex electric permittivity of the given constituent metals are $\varepsilon_{Pb} = -1.80\times10^{3} + 1.65\times10^{5} i$, $\varepsilon_{Al} = -3.40\times10^{4} + 1.34\times10^{6} i$,and $\varepsilon_{Ag} = -2.50\times10^{5} + 2.15\times10^{6} i$ [29,30]. The imaginary part of permittivity ε_{im} shows a monotonic increase from Pb, Al, to Ag. By noting the measured results shown in Fig. 1, the LC resonance for different constituent metals is seen to strengthen with increasing ε_{im}. Such a trend remains true at various given thicknesses, as shown in Figs. 1(a)-1(c). This is consistent with the recent numerical predictions at microwave frequencies . The electric permittivity of Ag, Al, and Pb can be well described by the Drude model as shown in the above equations. Our THz-TDS result agrees well with this simplified Drude expression, in that ε_{im} is proportional to the dc conductivity σ_{dc}, suggesting that the LC resonance is more pronounced with metamaterials of higher conductivity.

Furthermore, when the contribution of the real part of the permittivity ε_{rm} is considered, the LC resonance is found to be enhanced with an increasing ratio of the real to the imaginary permittivity, $-\varepsilon_{rm}/\varepsilon_{im}$. It was shown that a better conducting metal is characterized with a higher ratio $-\varepsilon_{rm}/\varepsilon_{im}$ [29,30]. The experimentally determined frequency-dependent values $-\varepsilon_{rm}/\varepsilon_{im}$ for the constituent metals are shown in Fig. 5-2 in the frequency range of 0.1-3.0 THz. At 0.5 THz, the ratios are 0.011, 0.025, and 0.116 for

Pb, Al, and Ag, respectively [19]. As can be seen in Fig.. 1, the measured LC resonance is indeed strengthened with the increasing ratio $-\varepsilon_{rm}/\varepsilon_{im}$ at each given metal thickness. This again is consistent with the simplified Drude permittivity, where the ratio $-\varepsilon_{rm}/\varepsilon_{im}$ is inversely proportional to the damping rate Γ, with experimentally determined values of $\Gamma/2\pi$ being 43.9, 19.6, and 4.4 THz, respectively, for Pb, Al, and Ag [29, 30-32].

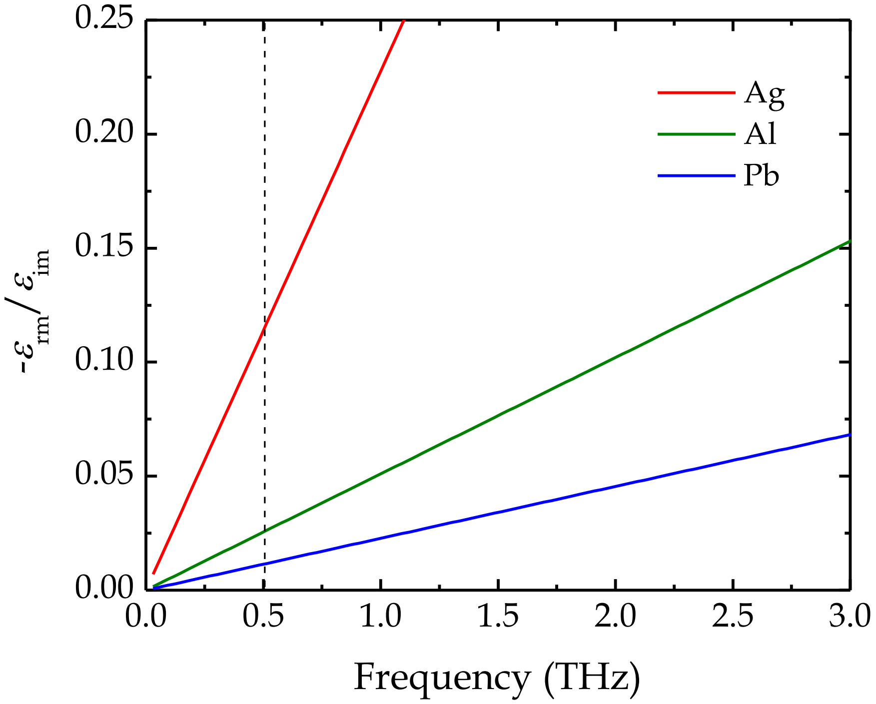

Figure 5-2 - Frequency dependent Drude ratio of the real to the imaginary permittivity, $-\varepsilon_{rm}/\varepsilon_{im}$ of Pb, Al, and Ag in the THz regime; the vertical dashed line indicates the LC resonance frequency 0.5 THz.

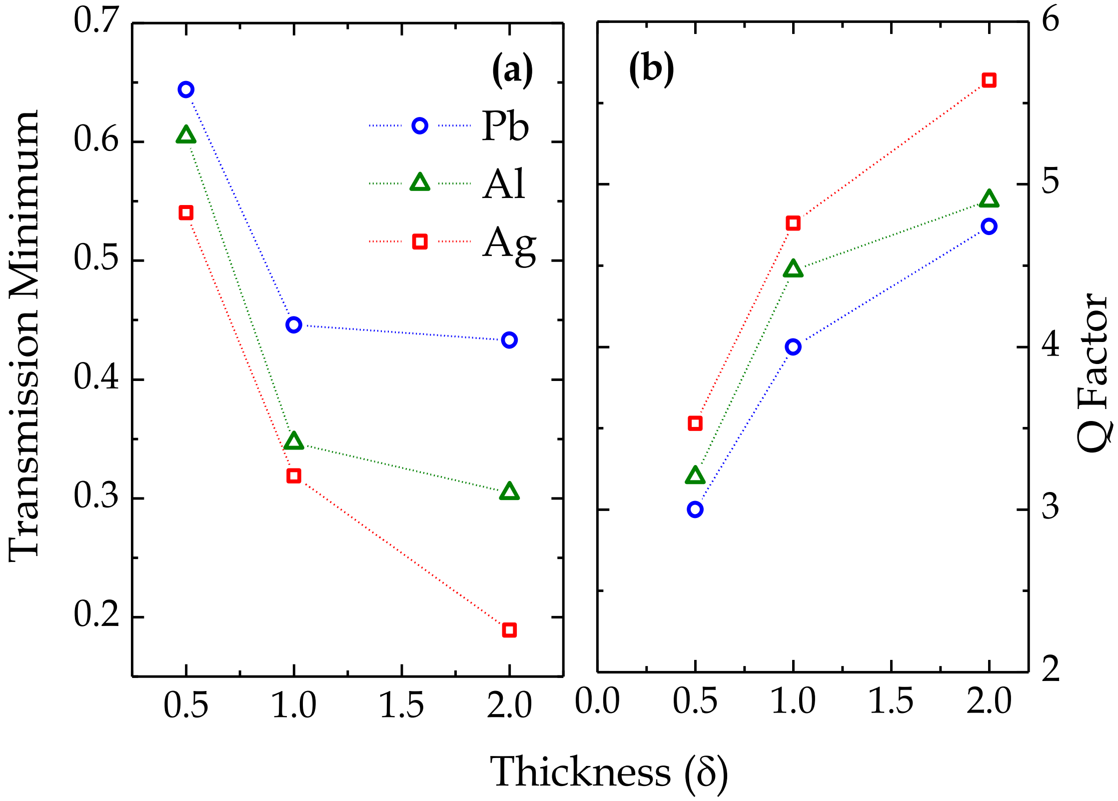

Figure 5-3(a) Measured dip amplitude transmission, and (b) Q factor at the LC resonance 0.5 THz for different metal SRRs with various thicknesses in skin depth.

In addition, the quality (Q) factor of the measured LC resonance also shows dependence on the permittivity of the constituent metals. The Q factor is a measure of the sharpness of resonance and is defined as the ratio of central frequency (f_{LC}) to the measured 3 dB power bandwidth ($f_{LC}/\Delta f_{3dB}$). As shown in Fig. 5-3(b), the experimentally extracted Q at the LC resonance shows an increasing trend with higher imaginary permittivity ε_{im}, as well as $-\varepsilon_{rm}/\varepsilon_{im}$. This relationship is limited, however, as the metal conductivity becomes very high. It is known that the SRR can be treated as an equivalent series RLC circuit. The Q of the RLC series circuit is inversely proportional to the resistance, $Q \propto 1/R$, where R is an effective resistance of the double SRR unit. However, SRRs are also radiators, continuously shedding resonant energy following excitation. Therefore the effective resistance can be expressed in two terms, the Ohmic resistance, R_L, and the radiation resistance, R_R , representing energy loss by heating and by radiation, respectively. At THz frequencies, the Ohmic resistance can be approximately given through the equivalent model [20]

$$R = 4l'/(th\omega\varepsilon_0\varepsilon_{im}), \text{ for } h < 2\delta \quad , \tag{5-6}$$

where h being metal thickness, and l' = 21 μm is the effective length of the SRR unit, and t being the metal width. The Ohmic resistance reduces with increasing ε_{im} or conductivity σ_{dc} of metals, thus increasing the Q factor. When the metal thickness approaches 2.0δ, the Q of the Ag metamaterial shows a 19% increase as compared with the Pb SRRs. The Q does not change as dramatically as ε_{im} due to the interplay of R_L

and R_R. As the conductivity increases, R_L becomes negligible compared to R_R. Further increases in ε_{im} or σ_{dc} do not affect R_R, and should result in very little improvement in Q.

The experimental results were supplemented by finite-element simulations [26]. Figures 5-4(a) and 5-4(b) illustrate, respectively, the measured and simulated amplitude transmissions of 300 nm thick SRR metamaterials made from different metals. Both the measured and simulated LC resonance reveals similar permittivity dependent behavior. The measured dip transmissions for the Pb, Al, and Ag samples are 47.7%, 25.5%, and 14.1%, respectively, showing a good agreement with the simulation results. The slight deviations in the simulated resonance frequencies may be caused by the approximation of defect-fee SRRs with frequency independent metal properties. In addition, we assume that the metal permittivity or conductivity is thickness independent; this is not necessarily true in reality [24,25].

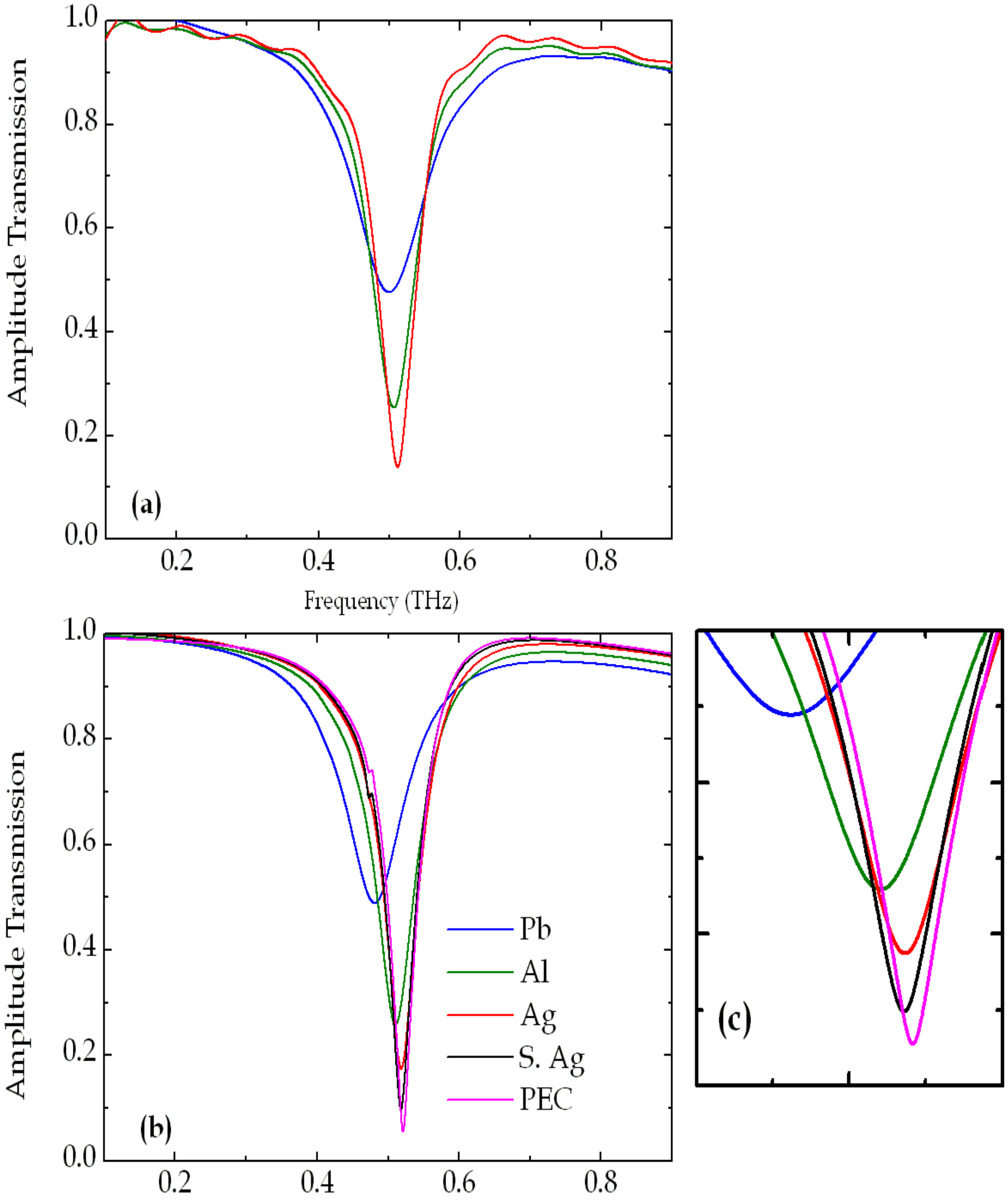

Figure 5-4 - (a) THz-TDS results and (b) Finite-element simulations of the LC resonant transmission of metamaterials made from 300 nm thick Pb, Al, Ag, S. Ag, and PEC. (c) blow off of the simulated LC resonance.

Importantly, the simulations enable an extrapolation of measured results. Fig. 5-4(b) shows the simulated transmission for SRRs made from a hypothetical metal having conductivity an order of magnitude higher than that of the regular Ag, here referred to as super Ag (S. Ag), and SRRs made from a perfect electric conductor (PEC). As expected, the resonance strength increases as ε_{im} increases and $R_L \to 0$. However, the improvement in Q is clearly saturated, verifying that radiation resistance is the dominant factor in limiting Q for SRRs of very low loss.

5. 6 Summary of Results

In conclusion, the resonant transmission of SRR metamaterials is shown to be dependent on electric permittivity of constituent metals. The measured LC resonance is strengthened with an increasing ratio of the real to the imaginary permittivity of metals at THz frequencies. The optimal transmission dip and Q-factor are observed in SRRs made from Ag, a highly conducting metal, though Q is effectively saturated due to the radiative nature of the SRRs. More interestingly, metamaterials made from Pb, a generally poor metal, also exhibit strong LC resonances due to a large permittivity in the THz regime. It thus indicates that THz metamaterials operate well over a wide range of constituent metals. This is essential in metamaterial applications involving integrated THz components, such as filters and modulators, when fine control of resonant properties is needed with a fixed layout design.

CHAPTER VI

THE IMPACT OF NEAREST NEIGHBOR INTERACTION ON THE RESONANCE OF THz METAMATERIALS

6. 1 Introduction

In this chapter we try to investigate the consequences of bringing the split ring resonators in close vicinity of each other and the impact which it has on its resonators due to their near field interactions [33]. It turns out that there is huge spectral reshaping of the higher order resonances of the split rings when their orientation is changed and their distance from each other is reduced. Tuning the resonance position of all modes by appropriate geometry modifications is usually at the focus of interest. But also the impact of the chosen period as well as the disorder was investigated. Nevertheless, a systematic investigation of how the orientation of the SRR in the unit cell affects the spectral response is addressed in this chapter.

We analyze here the impact of the orientation of the SRRs in the unit cell on the spectral position and the width of the resonance at normal incidence. MMs composed of three different super-cells containing four SRRs. The geometrical arrangement of the SRRs in each super-cell is shown in Fig. 6-1. In a first sample, all SRRs have their gap on the same side. In a second sample, the SRRs are arranged with vertical mirror symmetry, hence creating pairs of SRRs with facing gaps. In a third sample the SRRs have the same orientation of their gaps along the diagonal directions of the super-cell, hence next neighbors have their gap on opposite sides. In this work the effect of the orientation on the spectral position and the width of each resonance are investigated. It will be shown that the two lowest order modes are only marginally affected, whereas the higher order eigenmode suffers a severe spectral reshaping that depends strongly on the period. Quality factors as large as 18.5 are observed, being much larger than those usually encountered for THz MMs. As a consequence, it is shown that control over the orientation of the SRRs and the periodicity allows to observe extremely sharp features in the spectrum that are promising candidates for various practical applications such as sensing devices as well as for the fabrication of MMs that make explicit use of higher order resonances to control light propagation.

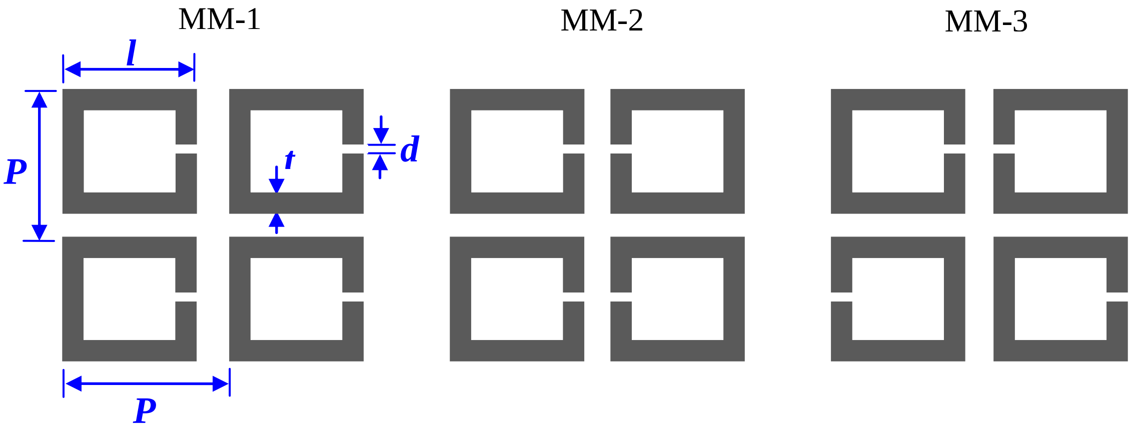

Figure 6-1 - Arrangement of super-cells MM1-MM3 with lattice constant *P* = 50 μm. Individual SRRs have dimensions of *t* = 6 μm, *d* = 2 μm, and *l* = 36 μm.

6. 2 Sample design and simulations

Six samples of planar SRRs (denoted in the following as MM1-MM6) of 200 nm thick Al metal rings were fabricated by conventional photolithography on a silicon substrate (0.64-mm-thick, n-type resistivity 12 Ω cm). As shown in Fig..6-1, MM1-MM3 are single ring SRRs with lattice constant P = 50 μm. The distribution of the gaps can be deduced from the Figure and corresponds to the scenarios as described before. MM4-MM6 are single SRRs with same symmetry as MM1-MM3 but with reduced periodicity of P = 39 μm. The dimensions of the SRR are t = 6 μm, l = 36 μm, and d = 2 μm. The orientation of the SRRs is such that either the THz electric field is parallel or perpendicular to the gap-bearing sides of all SRRs. Altering this orientation in a super-cell is not of interest as the SRRs resonances are spectrally decoupled and the interaction among neighboring elements is suppressed at all, though also the filling factor is effectively significantly decreased.

The exact parameters of the fabricated samples were motivated from numerical simulations of the optical response of the devices. Simulations were done with the Fourier Modal Method [34]. All geometrical parameters of the system were taken into account. Figure 6-2 shows the transmission for the three conFig.urations as a function of the period and the frequency. In all cases the incident E-field is polarized perpendicular to the gaps. The main peculiarities we can elucidate and which we will discuss in depth once the experimental results are shown are the following: (1) the impact of the conFig.uration and (2) the impact of the period for each conFig.uration on the spectral positions and the widths of the resonance; and (3) the occurrence of coherent phenomena once SRRs are closely spaced arranged. In the physical interpretation we subsequent provide we rely mainly on the selected experimental conFig.urations. The transition between the different scenarios can be inferred from this simulation.

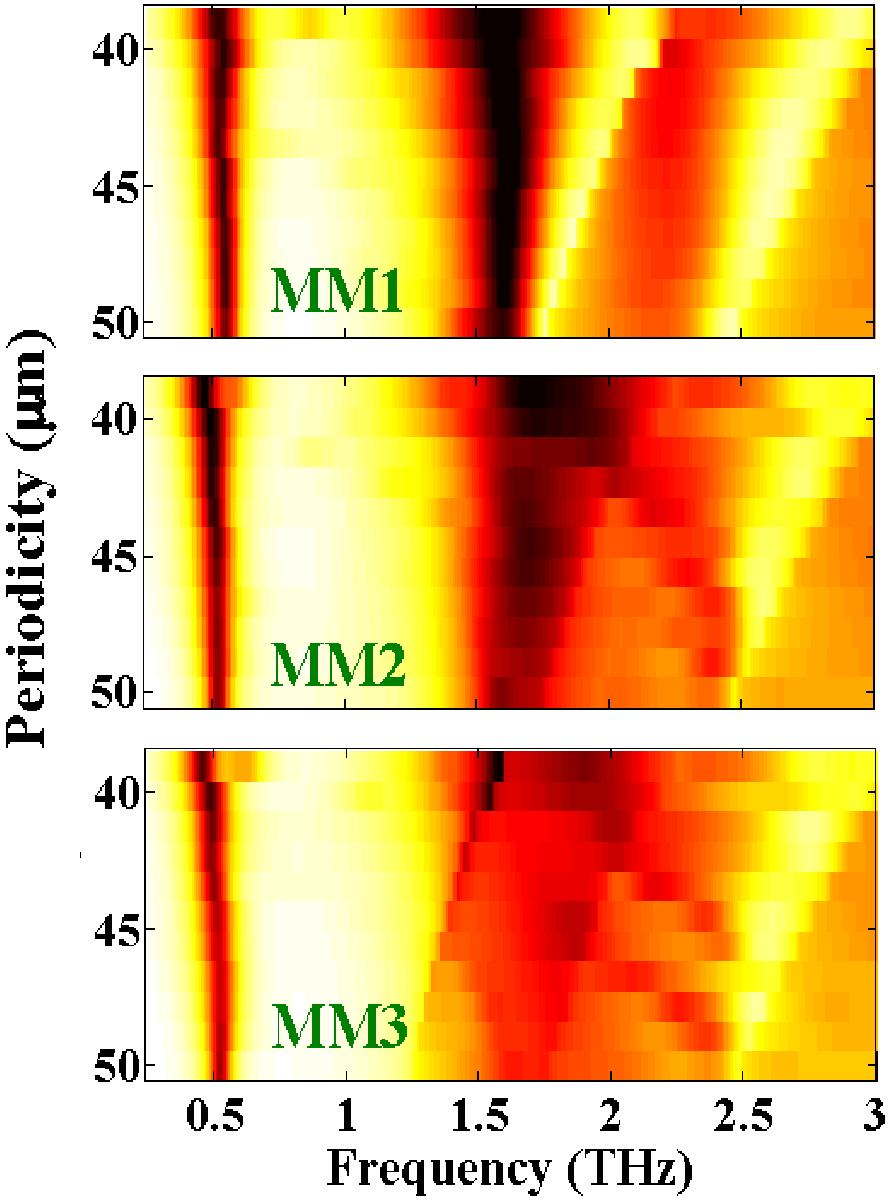

Figure 6-2. (Color online) Simulated transmission of samples MM1, MM2 and MM3 as a function of the periodicity for an incident E-field perpendicular polarized to the gap-bearing sides of the SRRs.

6. 3 Experimental Measurement

The measured time domain picosecond pulses that passed through MM1-MM3 and their Fourier transform are shown in Fig.s. 6-3a and 6-3b, respectively. In the pertinent measurements the electrical field is oriented perpendicular to the gap-bearing sides. The reference is a blank silicon slab identical to the substrate. The measured amplitude transmission of MM1-MM6 is shown in Figs. 6-4a, 6-4c and 6-4e and their respective simulation counterparts is shown in Figs. 6-4b, 6-4d, and 6-4f. The transmission is extracted from the ratio of the amplitude spectra of the samples to the reference $\left|\tilde{t}(\omega)\right| = \left|E_{sample}(\omega)/E_{reference}(\omega)\right|$. The two significant dips in transmission of Fig. 6-4a are traces from the two lowest order odd eigenmodes. Significant differences in the spectra are observed depending on the orientation of the gap of neighboring SRRs, direction of the incident electric field and the periodicity of each MM array.

When comparing the resonances of MM2 with those of MM1, it can be seen that the LC resonance at 0.5 THz is red-shifted by 20 GHz and the transmission is reduced by 4%. Contrary, the next higher order odd resonance at 1.5 THz broadens significantly, blue shifts by 84 GHz, and the transmission increases from 12.5% for MM1 to 30.1% in MM2. Furthermore, the orientation of the SRRs in the super-cell for MM3 causes only a marginal additional red shift of the lowest order resonance by 8 GHz and nearly no change on transmission. On the contrary, the next higher order resonances suffer from a severe broadening and a significant increase in transmission up to 49%.

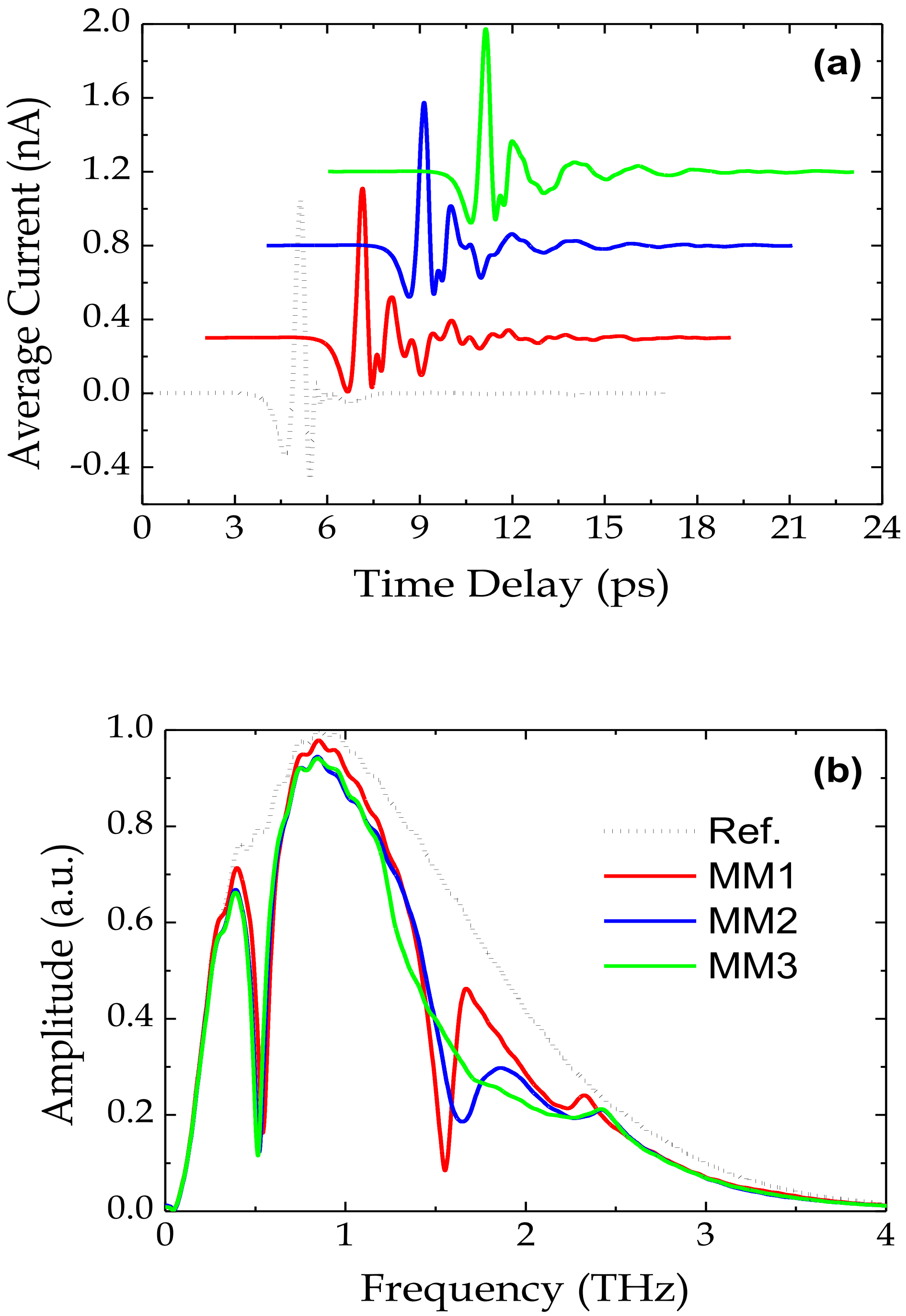

Figure 6-3 - THz pulses in the time domain (a) and in the frequency domain (b) of samples MM1-MM3.

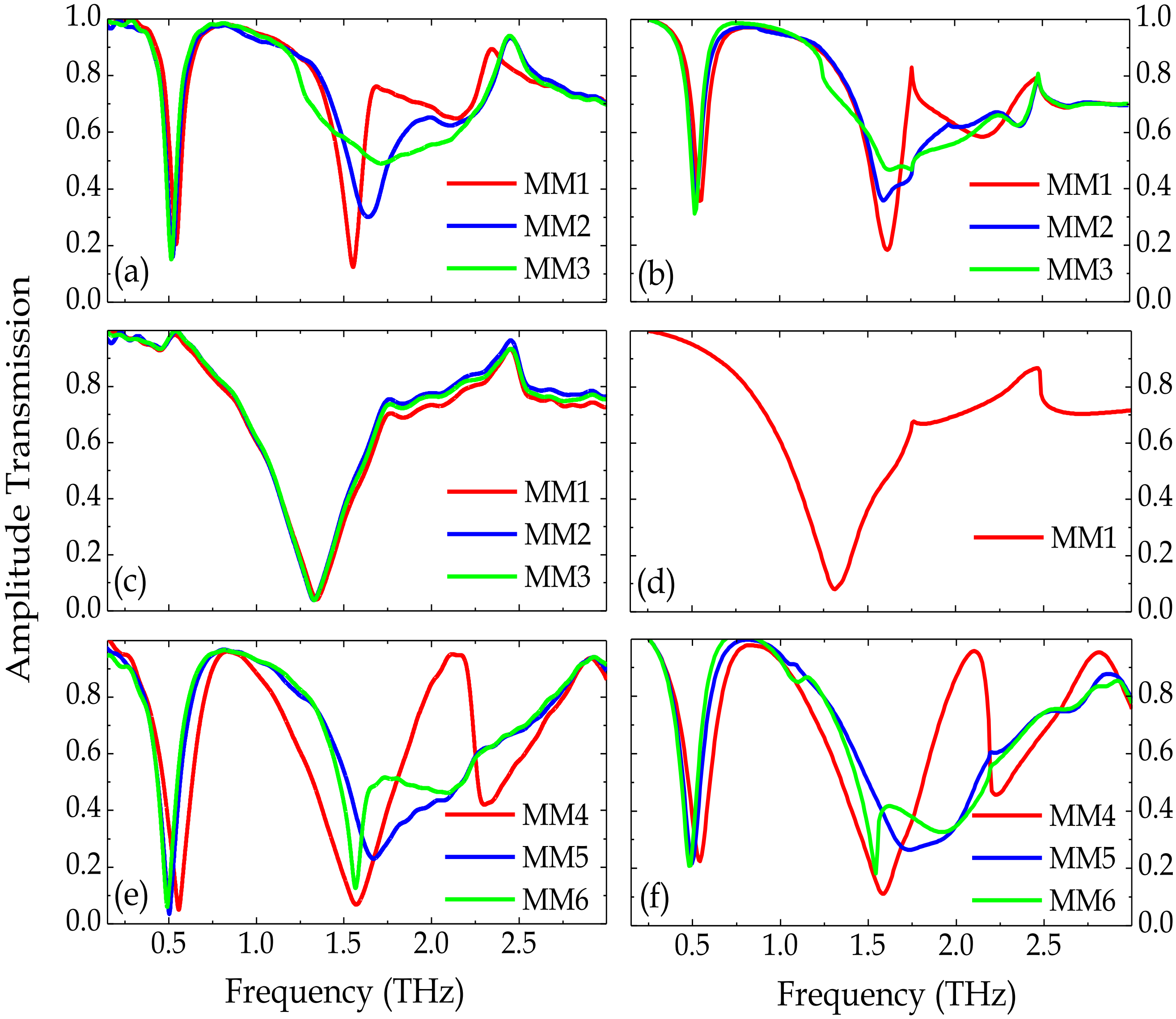

Figure 6-4. (Color online) (a) Measured and (b) simulated transmission spectra of samples MM1-MM3; the incident E-field is polarized perpendicular to the gap-bearing sides of the SRRs; (c) measured spectra of MM1-MM3 and (d) simulated spectrum of MM1 with the incident E-field polarized parallel to the gap-bearing sides; (e) measured and (f) simulated spectra of MM4-MM6.

For an incident electrical field parallel to the gap-bearing sides the response of MM1-MM3 is shown in Fig.. 6-3(b). Independent of the arrangement all spectra show a strong resonance at 1.33THz and have nearly the same spectral dependency. This resonance is related to the lowest order even eigenmode. Prior to the discussion of the physical conclusions, we show the experimental results for the samples with a period of P = 39 μm.

The transmission spectra for MM4-MM6 with reduced periodicity and high density of SRRs we observe a different spectral behavior in comparison with the samples MM1-MM3. In MM4 there are three distinct resonances, the LC resonance at 0.556 THz with a line width of 167 GHz, the next higher order odd eigenmode at 1.57 THz with a line width of 494 GHz and a third strong resonance at 2.3 THz. This resonance, however, is a Wood anomaly where the lowest diffraction order in the substrate changes its character from being evanescent to being propagating. This resonance is of no particular interest for the present study and will not be discussed further. In MM5 the lowest order odd eigenmode, the LC resonance, appears red shifted by 54 GHz and has a reduced line width of 125 GHz when compared to MM4. The next higher order odd eigenmodes is broadened and blue shifted by 100 GHz. In MM6 the lowest order odd eigenmode is again only marginally further red shifted by 11 GHz. The line width is reduced down to 115.5 GHz. Finally and potentially most interesting, the next higher order odd eigenmode appears as an extremely sharp feature with a line width of only 69.5 GHz; resonating approximately at the same frequency as the higher order odd eigenmode of MM4. The resonance has a Q-factor of only 18.5. Upon illuminating the samples with an electric field polarized perpendicular to the gap, again no influence of the SRR’s arrangement on the spectral response was observed. Results are omitted for brevity.

6. 4 Discussion and Analysis

To explain the influence of the arrangement on the spectral properties of the lowest order eigenmode one may evoke analogies to transmission line theory [36]. Placing SRRs like in MM2 and MM4 such that the gaps of next neighbors face each other will cause an increase of the effective capacitance as the next neighbor in such situation provides a parasitic capacitance in parallel. The increase in effective capacitance causes a reduction of the eigen frequency and a decrease in radiation losses, hence decreasing the line width. If furthermore, as in the transition from MM2 to MM3 or MM5 to MM6, the SRRs in the direction parallel to the gap have an alternating orientation, the parasitic capacitance in parallel is reduced, hence increasing furthermore slightly the effective capacity of the SRR. Nevertheless, the impact of this rearrangement is not as pronounced, as only a marginal further reduction of the resonance frequency and the line width for this second transition can be seen.

Seemingly, for the second resonance; the lowest order even eigenmode that is excitable with the illuminating electric field polarized perpendicular to the gap-bearing sides; the placing of the gap on either side of the SRR has no influence. This is perfectly explainable as this mode is dominantly characterized by oscillating currents in the side arms of the SRR that have no gap. Therefore, no modification of the resonance conditions for the SRR is neither observed nor expected. As a consequence, the spectral position and the width of the resonance is the same for all conFig.urations.

For the third resonance; being the second order odd eigenmode [37]; the situation is more involved, as seemingly the resonance shape and position depends on the chosen period and consequently on the absolute distance between neighboring SRRs. By taking into account that the resonance wavelength is comparable to the chosen interparticle distance, we presume that the coherent superposition of the scattered field by neighboring SRRs causes the strong modification of the transmission in this spectral domain. The formation of a subradiant and a superradiant type mode, depending on the interparticle distance and the gap orientation, causes a blue-shift or a red-shift of the resonance [38]. The superradiant (subradiant) mode also increases (decreases) the radiation losses of the excited eigenmode which leads to a broadening (narrowing) of the spectral resonance as encountered.

6. 5 Summary

To summarize, we have investigated the impact of gap orientation of neighboring SRRs on the spectral properties of the resonances that are excitable in such systems. It was shown that by choosing an appropriate orientation the lowest order eigenmode is shifted towards lower frequencies and suffers from a decrease in radiation losses, causing the line width to be much narrower. The effect was explained in terms of an increase of the effective capacitance of the SRR by a proper increase (decrease) of the parasitic capacitance that is induced in parallel (serial) by neighboring SRRs. As this resonance is usually used to evoke a strong dispersion in the effective permeability, the approach might open an avenue towards MMs with an even stronger material dispersion at a better ratio of resonance wavelength over period by fabricating SRRs with nominal the same size. It was furthermore shown that, potentially due to a strong coherent coupling between the fields scattered by neighboring SRRs at the next higher order odd eigenmode, the resonance experiences a significant reshaping depending on the distance and sharp spectral features do occur. Such sharp resonant features, obtained due to coupling in MMs, can open up possibilities for the use of MMs as highly efficient sensing devices [39] and also provide a better understanding of SRRs arrays with different symmetry layouts. Overall, resonance coupling reveals a method to engineer the MM spectrum in a controlled and predictable way across the entire EM spectrum.

CHAPTER VII

RANDOM THz METAMATERIALS

7. 1 Introduction

In this chapter we investigate the normal incidence transmission through periodically and aperiodically arranged planar SRRs. Most of the previous works on metamaterials were focused on investigating the unique properties of wave propagation through periodic structures. There has been a tremendous curiosity to explore the collective behavior of SRRs when a disorder sets in either their geometrical dimensions or periodic positioning on the host media [40-43]. An in depth understanding of the influence of randomness on the electromagnetic properties of SRRs can further open the doors towards the development of negative index materials in a broad spectrum of electromagnetic waves.

To address the question of how tolerant the metamaterials are to the destruction of their positional periodicity we investigate the transmission properties of THz radiation as it propagates through the disordered SRRs. We find in this particular set of experiment that the introduction of positional disorder in metamaterials has no effect on its fundamental Inductive-Capacitive resonance. The lowest order even and the second order odd eigen modes undergo broadening and shift in their resonance frequencies. The experiment reveals that the left handedness in THz metamaterials is not affected by the random positioning of SRRs.

7. 2 Definition of randomness in this experiment

The random medium here is characterized by *f*, the volume fraction occupied by the metal from which the split rings were made. The disorder was introduced by manually changing the lattice points of SRRs randomly during the mask design making sure that the SRRs do not touch one another. Each of the periodic SRRs was initially at a lattice position, $\vec{r}_n$, where $\vec{r} = x\vec{i} + y\vec{j}$ and each SRR was displaced by $\pm\vec{\delta x}$ and $\pm\vec{\delta y}$ to introduce positioning disorder, where $\delta r = \delta x\vec{i} + \delta y\vec{j}$, is used to define the degree of randomness [40].In our case $\left|\vec{\delta x}\right| \leq 32\mu\text{m}$ and $\left|\vec{\delta y}\right| \leq 32\mu\text{m}$, leading to a maximum disorder $\left|\vec{\delta r}\right| \leq 45.25\mu\text{m}$, which is equivalent to 85% of the periodicity, P=53μm. The random SRRs retain the number density as that of the counterpart periodic SRRs, giving the metal volume filling fraction, *f* = 0.252 for the single SRRs, MM1 and MM2 and *f* = 0.35 for the double SRRs, MM3 and MM4 as shown in Fig. 7-1.

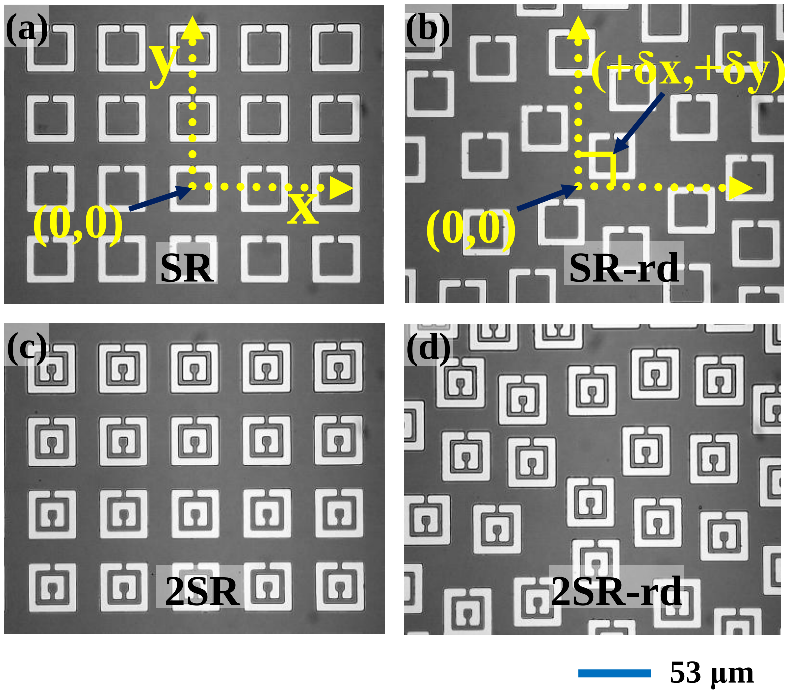

Figure 7-1 - (a)-(d)Lithographically fabricated single and double periodic and random split ring resonators (MM1-MM4) with180nm Al SRRs deposited on n-type silicon substrate, (e)the schematic diagram of the double SRR unit with dimensions *w* = 3 μm, *t* = 6 μm, *l* = 36 μm, *l'=21* μm, *d* = 2 μm, and the periodicity is *P* = 53 μm.

7. 3 THz – TDS characterization

Figures 7-2a and 7-2c shows the measured time domain pulses transmitted through the reference and the single SRRs, MM1 and MM2 for the corresponding Fourier transformed spectra for the E field oriented parallel and perpendicular to the gap bearing side respectively. The frequency domain spectra of MM1 as shown in Fig. 7-2b and Fig. 7-3a reveals mainly three resonant features. The lowest order odd eigenmode or the so called LC resonance occurs at 0.54 THz with a 20.3% transmission minimum and resonance line width (FWHM) of 79 GHz, the second order odd eigenmode is at 1.56 THz with 12% transmission, and a 117 GHz line width and the third is the weaker resonance at 2.12 THz which is due to the Wood's anomaly. As shown in Fig. 7-2d, the lowest order even eigen mode resonates at 1.34 THz. For sample MM2 in the parallel orientation there is no change observed in the LC resonance feature compared to that of MM1.The next higher resonance, however blue shifts by 16 GHz, the line width broadens by 80 GHz and transmission is significantly modified from 12% to 28%.In perpendicular orientation the lowest order eigen mode of random structure, MM2 red shifts by 34 GHz and broadens by 106 GHz. This behavior indicates that the higher frequency resonances are clearly affected by the positioning randomness of SRRs. The modification of high frequency resonance behaviors in the random SRRs can also be revealed from the time domain pulse, which has less ringing features towards longer delay time beyond the second peak.

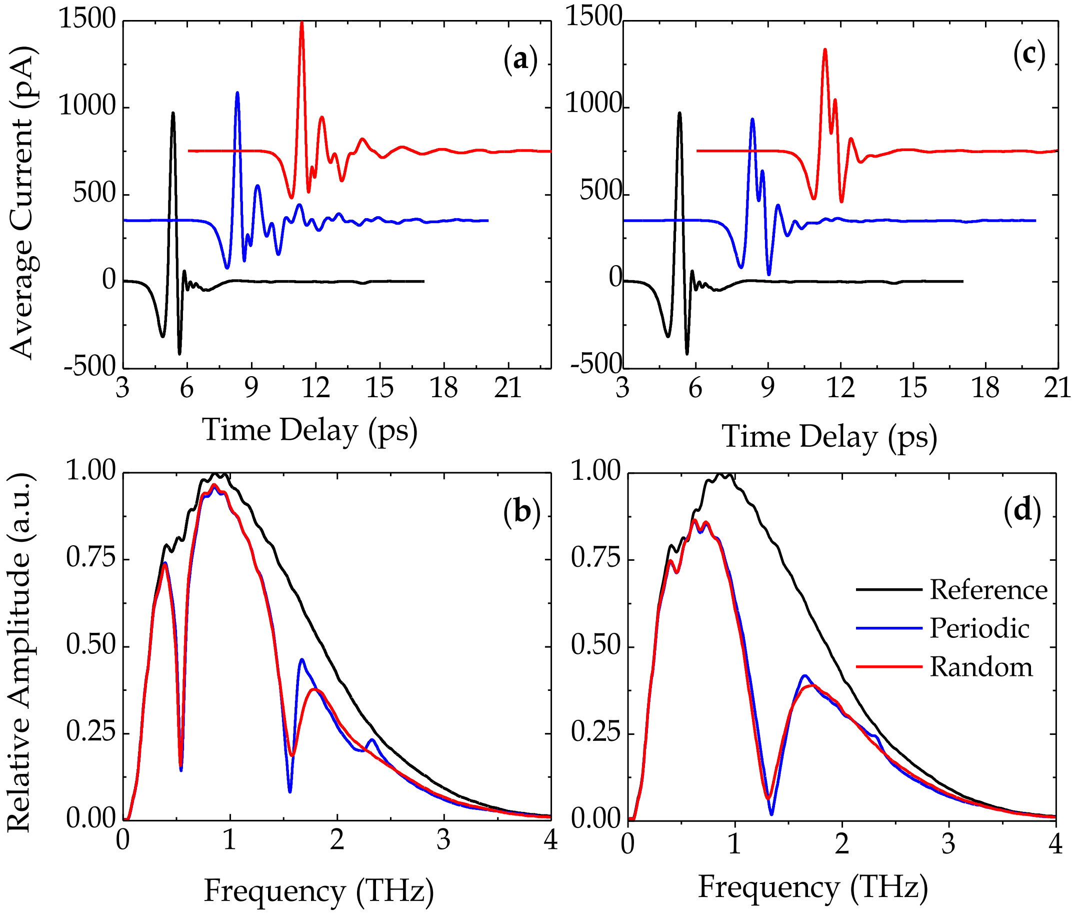

Figure 7-2 - (a) Measured time domain Pico-second pulses and (b) Frequency spectrum of blank Silicon substrate, periodic single ring SRRs, MM1 and random single ring SRRs, MM2; E field is along the gap of SRRs. (c) Time domain pulse and (d) spectra for blank Si substrate, periodic double ring SRRs, MM3 and random double ring SRRs, MM4; E field is perpendicular to the gap bearing arms of SRRs.

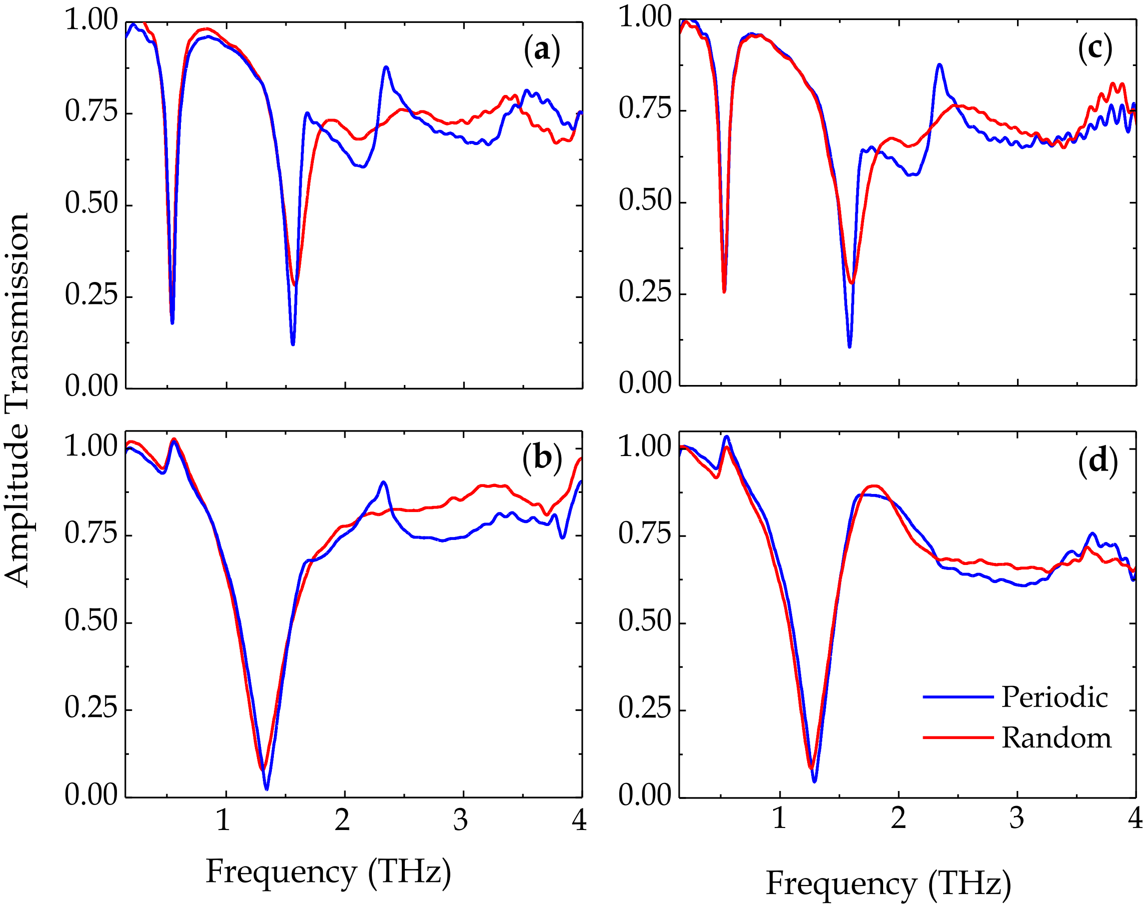

Figure 7-3 - (a) and (b) Measured Transmission Spectrum of MM1-MM2 and (c) and (d) of MM3-MM4 for parallel and perpendicular polarizations respectively.

Figures 7-3a and 7-3b shows the amplitude transmission for MM1-MM2 and Figs. 7-3c and 7-3d for MM3-MM4. The frequency dependent complex THz transmission is extracted from the ratio of Fourier transformed sample and reference measurements, $t(\omega) = \left|E_{sample}(\omega)\right| / \left|E_{reference}(\omega)\right|$. From the transmission spectra we found similar results with the periodic and random double SRRs as that of the single SRRs. The LC resonance of MM3 and MM4 were identical in all respects. The second resonance at 1.58 THz blue shifted by 16 GHz, broadened by 99 GHz from 0.109 to 0.208 THz and the resonance minimum decreased by 17.5%. The lowest even eigen mode red shifts by 28.5 GHz and broadens by 49 GHz.

7. 4 Discussion and analysis

The LC resonance is independent of randomness in the positioning of SRRs as its peak frequency and resonance strength remain unaffected. The resonance arises due to the circular current distribution in the metallic arms of the SRRs. SRRs can be treated as an equivalent RLC circuit in which the resistance, R comes from the resistive metal arms, inductance arises from the current circulating around the SRR perimeter and capacitance, C is due to the accumulation of charges across the SRR gaps. The amount of current circulating depends on the impedance of the SRR metal arms. The LC resonance strength can only be altered if the impedance of the SRR changes. The equivalent resistance of a single SRR can be modeled by equations 4-5. All the parameters which determine the resistance of the rings remain unchanged for the periodic and their corresponding random counterpart structures, leading to the same current distribution profile in them. The only difference between them being the displaced position of the current loops in the random SRRs. The collective response of all random SRRs at LC resonance remains identical to their periodic counterpart as long as their number density is not changed greatly and number density is taken care of by having the same volume filling fraction. The coupling between the individual elemental SRR is tolerant to the positional variation and so the resonance dip and line width does not change at all for the random case. The LC resonance of SRRs has the form

$$\omega_{LC} = \frac{c_0}{l\sqrt{\varepsilon_c}}\sqrt{\frac{d}{t}} \quad , \tag{7-1}$$

which is determined primarily by the size of the rings, where, ε_c is the permittivity of the boarding material across the capacitive gap and c_0 is the velocity of light. The geometrical size of the SRRs is not changed while randomizing the structures which ensure that the inductance and capacitance of SRRs in even the disordered samples remains constant. This explains the reason for not being able to see a shift LC resonance frequency for the randomly placed structures.

Unlike the LC resonance, the higher frequency plasmon resonances in random structures undergo a change. This can be expected due to different current profiles the SRRs have at LC and at the other resonance frequencies. The second odd and lowest even eigen mode resonances in the transmission spectra of all the SRRs have similar current density distributions and therefore those resonances undergo similar spectral change when randomness is introduced in SRRs. The incident THz electric field excites plasmon oscillations of conduction electrons at the surface of individual metallic SRR arms that are parallel to the illuminating field, producing a collection of oscillating dipoles with dipole moment, $p(t)$ .The electric field of an oscillating dipole consists of near field, intermediate field, and far field components and is expressed as

$$E(r,t)=\frac{1}{4\pi\varepsilon_0}\left(\frac{p(t)}{r^3}+\frac{1}{r^2c_0}\frac{\partial p(t)}{\partial t}+\frac{1}{rc_0{}^2}\frac{\partial^2 p(t)}{\partial t^2}\right) \quad , \qquad (7\text{-}2)$$

with r being the distance from the dipole. The dipole resonance is due to the dipole-dipole interaction between the SRR arms in the direction of incident E field**.** The mechanism of dipole-dipole interaction and coupling depend on the distance between them as stated in the above equation. In the case of periodic metamaterial structures the coupling between the dipoles is strong at an appropriate periodicity. In the randomly distributed SRRs, however, the interaction between the oscillating particles is partially cancelled by the disorder, which leads to weaker coupling among the dipoles. As a result we observe broadened and weak plasmon resonances at higher frequencies in the randomly scattered SRR metamaterials [44].

7. 5 Summary of results

In conclusion, we have investigated the propagation of electromagnetic waves through disordered metamaterials at THz frequencies. We experimentally demonstrate that the spectral location, the line shape and the strength of the LC resonance of single and double randomly spaced split ring resonators remain unchanged when compared to their periodic counterparts having the same volume filling fraction. The circular currents in the split rings couple equally well in random SRRs as in the periodic SRRs. The losses are observed only at the higher order plasmonic resonances and they become weaker in random SRRs due the weak coupling between the randomly scattered oscillating dipoles. This finding reveals that the random SRRs can not only be effective in obtaining negative refraction in THz domain but also at all frequencies of the electromagnetic spectrum.

CHAPTER VIII

THIN FILM SENSING WITH PLANAR THz METAMATERIALS

8. 1 Introduction – Sensing aspect

The continued quest for new chemical and biological sensing modalities that avoid labeling, improve sensitivity, and take advantage of new chemical signatures has fueled a recent interesting THz, or far-infrared, sensing [45]. This is mainly due to the unique properties many materials exhibit in the THz regime. Of particular interest are those materials that respond resonantly at THz frequencies, making them more amenable to sensing in small quantities. Some examples include explosives [46,47] and DNA [48]. Detection techniques for sensing very small quantities at THz frequencies have also matured. For example, waveguide sensors have proven useful for sensing thin films of water [49] by increasing the effective interaction length. In other examples [50–55] THz micro-resonators and filters were studied to sense analytes by the frequency shift they induce on the device's resonant response.

This method is reported to have increased sensitivity to the binding state of DNA samples by 103 times over conventional free-space time-domain spectroscopy. Metamaterials and frequency selective surfaces have also arisen as candidates for highly sensitive chemical or biological detection since they can be small (unit cell dimensions are typically $\lambda/10-\lambda/5$) and show a resonant frequency response that is tunable by design. It has already been shown that small quantities of silicon (< 1 ng), deposited as a film or over layer on a planar THz metamaterial, can shift the resonance frequency by an easily measurable amount [54]. Similarly, simulations of asymmetric split-ring resonators (SRRs) indicate a possible scenario in which films as thin as 10 nm may be measured [55]. These ideas capitalize on the structure of split-ring resonators, whose natural oscillation frequencies depend critically on the permittivity of the boarding dielectrics. Our work has shown good consistency with this principle: the resonance frequency of SRRs shifted from 0.80 THz to 0.51 THz by changing the substrate from fused silica to silicon. In terms of practical sensing, however, the limits of this technique are clearly important as they will ultimately define the utility of the sensing approach. Here we investigate the behavior of dielectric over layers on metamaterials, with particular relevance to sensing limitations. We first present measured THz transmission data illustrating the resonance shifting effects and then compare this to previous similar approaches. Finally, we discuss the implications in terms of practical sensing considerations.

8. 2 Experiment

The array of square SRRs, made from an optically thick 200-nm aluminum film, is micro-fabricated by conventional lithography technique on a 0.64-mm-thick silicon substrate (p-type resistivity 20 Ω cm). Double-ring SRR with a minimum feature d = 5 μm in the splits of the rings and other dimensions of w = 5 μm, t = 5 μm, l = 40 μm, and a lattice constant of P = 60 μm. Each SRR array has a 20 mm × 20 mm clear aperture. The dielectric layer on the SRR arrays is either spin coated by single-wafer spin processor (Laurell WS-400A) or deposited by thermal evaporator (BOC Edwards AUTO 306).

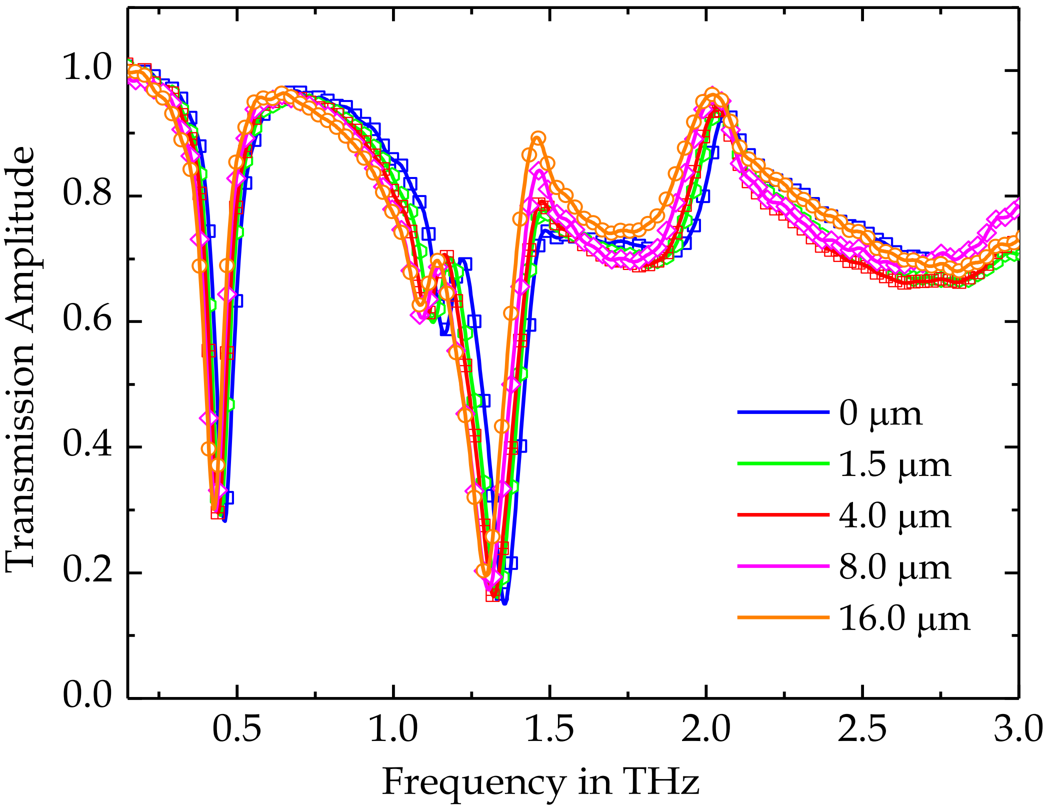

Figure 8-1 - Frequency-dependent amplitude transmission. The points are the actual measured data and the continuous lines are the zero padded curves. The E field of THz pulses is perpendicular to the SRR gaps.

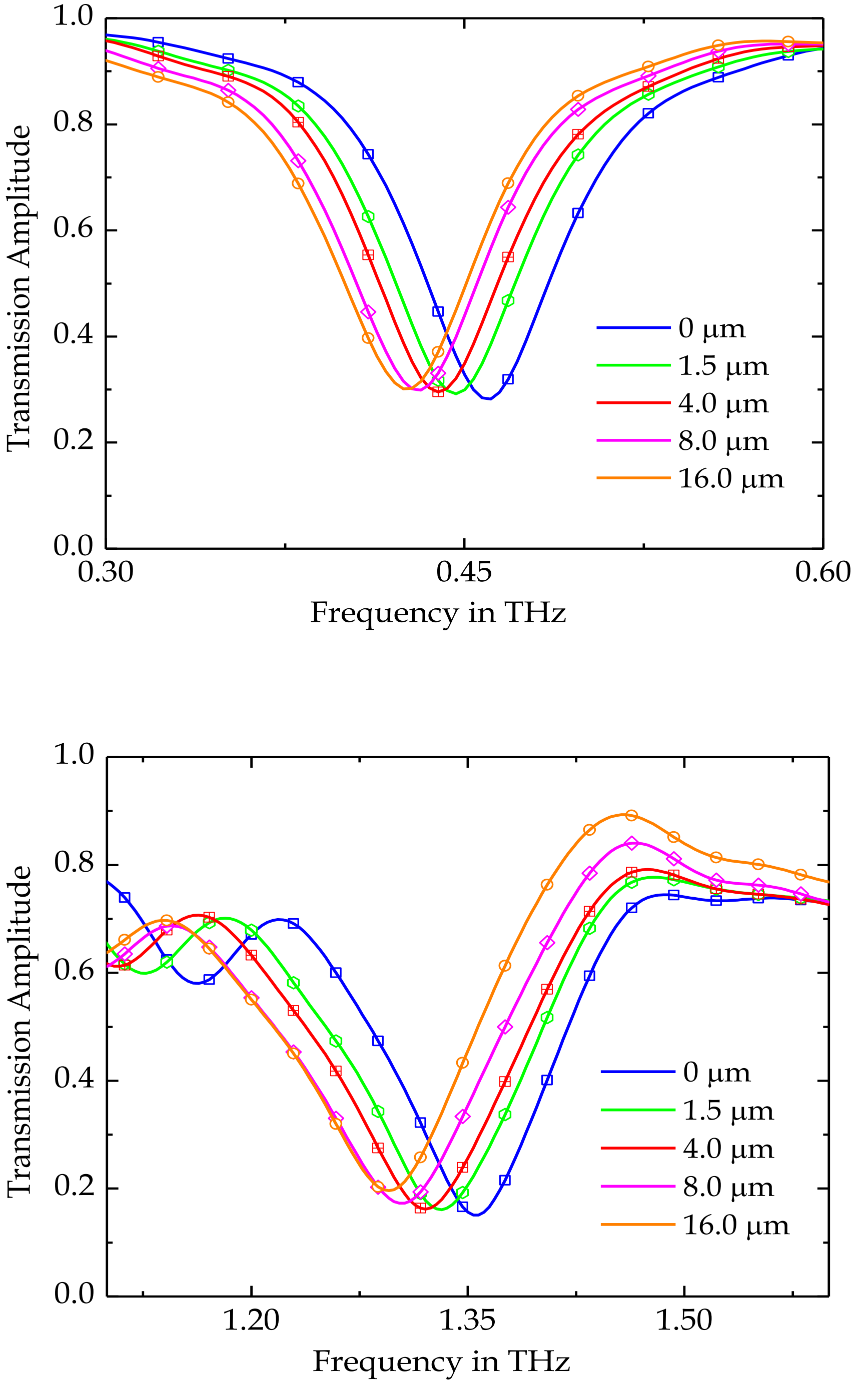

Figure 8-2 - Zoomed Frequency-dependent amplitude transmission at (a) LC resonance and (b) Dipole resonance; Dots are actual data and lines are zero padded data.

Figure 8-1(a) illustrates the frequency-dependent amplitude transmission of a planar SRR metamaterial without (solid curves) and with a dielectric layer made from a 16-μm-thick photoresist (Futurrex, Inc., dotted curves). The transmission is extracted from the ratio of the Fourier-transformed amplitude spectra of the sample to the reference; the latter being a blank silicon slab identical to the SRR substrate coated with the same thickness of dielectric layer as that on each sample. Two distinct resonance dips observed in the uncoated SRR array are the LC resonance ω_{LC} at 0.460 THz and the electric dipole resonance ω_0 at 1.356 THz. When a thin dielectric layer is applied on the surface of SRRs, a frequency shift is observed at both resonances. As shown by the dotted curve in Fig.. 8-1(a), with a 16-μm-thick dielectric layer ($\varepsilon_1 = 2.7 \pm 0.2$ at 1.0 THz), both the LC and the dipole resonances shift to lower frequencies by 36 and 60 GHz, respectively. Figure 8-1(b) shows the corresponding phase change obtained from the phase difference between the sample and the reference spectra. By having the derivative shape of the sharp resonances in the transmission, the phase change also clearly reveals the frequency red shift due to the effect of the dielectric overlayer.

The measured resonances ω_{LC} and ω_0 as a function of thickness of the dielectric layer are shown as open circles in Fig.s. 8-2(a) and 8-2 (b), respectively. As the thickness of the film changes from 1.5 to 16 μm, both resonances shift to lower frequencies. The LC frequency is tuned from 0.446 to 0.424 THz, while the electric resonance redshifts from 1.332 to 1.296 THz. The insets illustrate the corresponding amplitude transmission near the resonances with various film thicknesses. To further explore the redshift behavior of the SRRs, even thicker dielectric layers are applied. However, for film thicknesses varied from 16 to 90 μm, the frequency shift of both ω_{LC} and becomes saturated and we see no obvious change in the resonance frequencies.

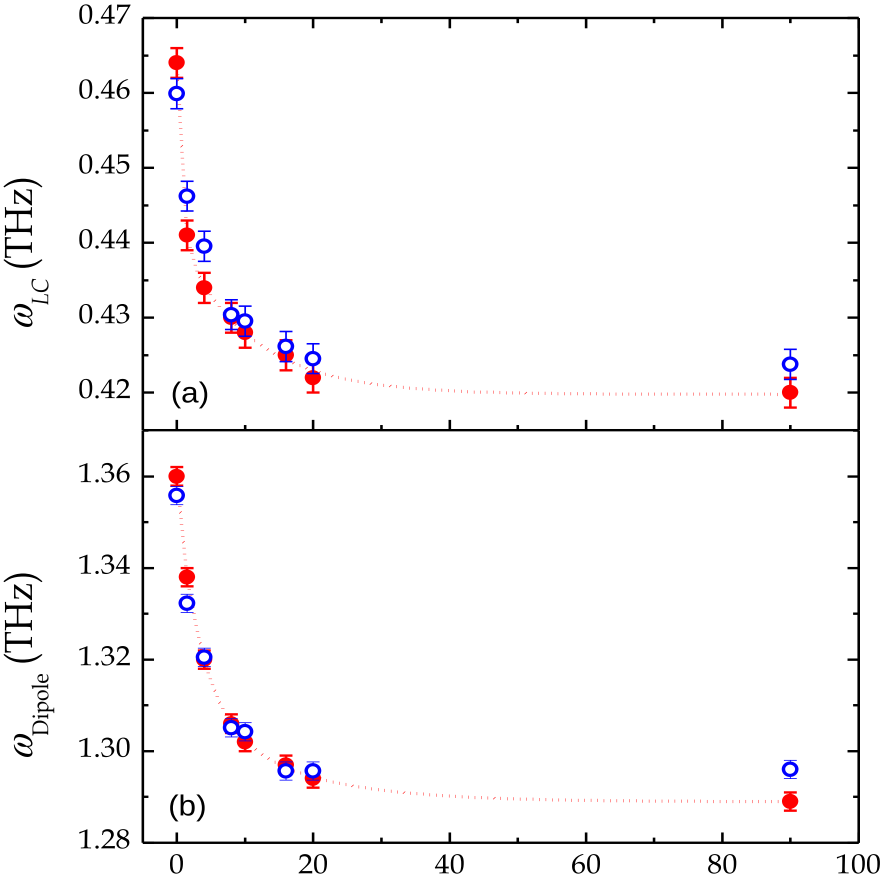

Figure 8-3 - (a) LC (ω_{LC}) and (b) electric dipole (ω_{dipole}) resonance frequencies as a function of thickness of the dielectric overlayer on SRRs. The measured (open circles) simulated (dots) results are represented by open squares and dots, respectively, with the dotted curves as a guide to the eye. The peak frequencies of both resonances are determined from the results of numerical fitting to the measured data by using zero padding [56].

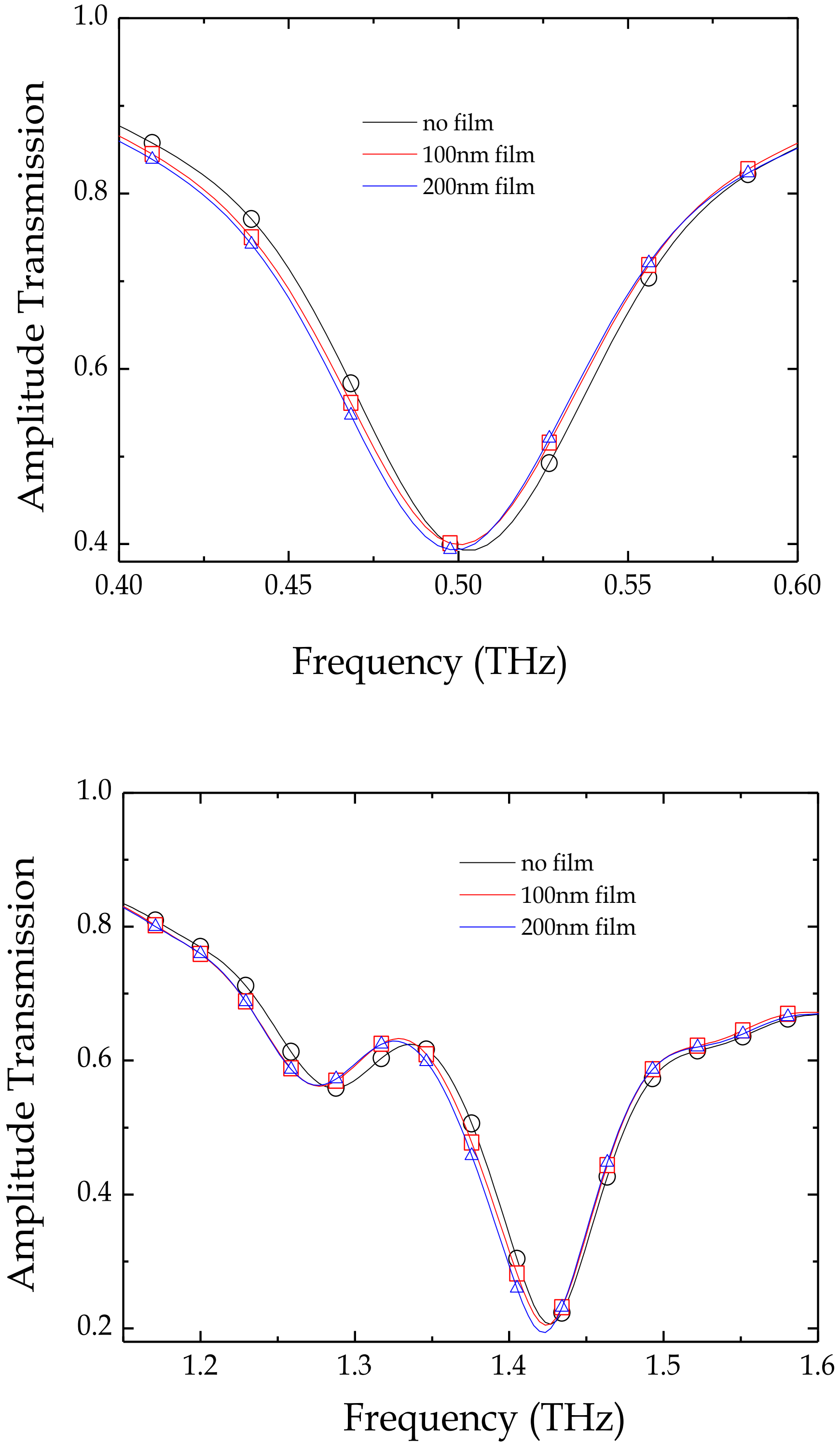

Figure 8-4 - Measured amplitude transmission at (a) LC and (b) Dipole resonances of a double-ring SRR metamaterial with a B_2O_3 nano overlayer film. The dots are measured points and lines are zero padded curves.

8. 3 Analysis

We now discuss the implications of the measured data with respect to sensing limitations inherent in these metamaterials. While a 2-3 GHz resonance shift is both measurable and repeatable in our data, it is certainly approaching the minimum measurable change for this experimental conFig.uration. Systems in which noise or sensor contamination is a larger issue would obviously require greater resonance shifts for positive identification. Since the measured resonance shifts were due to alterations in the SRR capacitance, one can formulate a quantitative approach to determining the limitations of SRRs as sensors. It begins by utilizing the RLC circuit model of the SRR, a valid and commonly used approach for describing SRR behavior. A 2 GHz resonance redshift corresponding to −0.4% (at 0.503 THz) is caused by a 0.8% increase in SRR capacitance. It is generally accepted that most of the capacitive response of a SRR occurs in a small volume surrounding the ring gaps. This is due to the strong field enhancement commonly observed there. However, our measured data shows that this enhancement is not quite as useful for sensing as it first appears. The 100 nm B2O3 over layer half fills all the regions (ring gaps and space between rings) bound by the 200 nm thick aluminum. Even with strong electric field concentration, this significant gap alteration only results in a 0.8% change in the net SRR capacitance.

The limitations to this sensing modality become apparent. A metamaterial array based on a high-permittivity substrate will have a large, and likely majority, capacitive contribution in the substrate. Obviously, the sensed layer cannot penetrate the substrate or interact with any of the electric flux contained therein. This substantially dilutes the change in capacitance and decreases the amount of resonance shift due to the overlayer. Though thinner substrates would certainly improve the situation, it's clear from the saturated resonance shift data of Fig.. 8-2 that a substrate of only 10-20 μm is sufficient to maximize this dilution effect. Such thin substrates obviously cause great fabrication and durability challenges. This is only one manifestation of the overarching limit to sensing with metamaterials: there is critical volume of electric flux which must be contained within the sensed layer to cause a measurable resonance shift. Yet another instance is revealed by the saturated resonance data. From Fig.. 8-2 we can surmise that SRR fringing fields extend out to roughly 16 μm. Again, this represents electric flux that is not contained directly within the SRR gaps. As such, any sensed layer confined to the gaps would have no interaction with this fringing flux, thus reducing its effect on the measured resonance. These considerations indicate that THz sensing of low-volume layers (i.e. single-molecule layers, functionalized receptor planes, low-density airborne species, etc.) using metamaterials on thick, high-index substrates faces a number of possible challenges, in spite of potentially large sample permittivities.

Given the limitations defined by the data we can estimate how much the situation could be improved by altering the metamaterial substrate. What follows is an extrapolation of the measured results that permits an estimation of the sensing limitations of our ring design. The same procedure could be applied to measurements of any similar metamaterial, however the specific numbers involved would change. The minimum sample volume which could be sensed with a substrate-free metametamaterial design (or free-standing metamaterial) can be approximated by first assuming that the electric flux distribution on either side of the plane of our Si-based SRR is spatially symmetric. The symmetry here refers only to the shape of the flux distribution, not its density, which is greater in the substrate due to its high permittivity. This implies that the substrate-bound flux accounts for roughly 90% of the total SRR capacitance. The total SRR capacitance is then modeled as four parallel capacitors: C_1 being the capacitance due to flux within the substrate, C_{2a} due to flux within the air filled fraction of the gap volumes, C_{2d} due to flux within the over layer filled fraction of the gaps, and C_3 due to fringing flux in air. If the 0.8% measured capacitance shift is due only to dielectric changes in the gap volumes, then it can be shown that $C_{2a}+C_{2d}$ only accounts for about 0.6% of the total SRR capacitance, C_0.

8. 4 Comparison with biosensor platform

Finally, it is useful to compare the sensitivity, advantages, and disadvantages of the device analyzed in this paper to more established label-free biosensor platforms, an issue commonly overlooked in THz oriented work. Most of the label-free biosensor platforms measure mass-loading over a finite sensing area, and thus sensitivities are quoted in units of pg/mm2. Examples of non-optical techniques include quartz microbalances and surface acoustic wave sensors, with reported sensitivities in the range of 5–200 pg/mm^2. A number of commercial optical biosensors have mass sensing resolutions ranging from 0.1–5 pg/mm^2 [57] over areas ranging from 50 μm^2 [56] to 23,000 μm^2 [58]. These mass resolution ranges allow detection of relatively small compounds (100’s of daltons (Da)) on larger immobilized targets (10’s of kDa). In DNA hybridization, one typically measures the addition of 7–10 kDa oligo fragments to immobilized short strands, but with very small changes in overall thickness .We can compare our device to these systems by knowing that the aforementioned mass-loading translates into a thickness resolution on the order of a few nanometers to achieve monolayer sensitivity to macromolecules. For example, a monolayer of BSA adsorbs with a thickness of 4.5 nm [59]. Adsorbed thickness is only 2 nm for 20-base long double-stranded DNA. The results of our experimental analysis show such fine thickness resolution is obviously unattainable with our devices. On the other hand, the THz regime offers large changes in permittivity associated with these macromolecule layers, a feature unavailable to optical sensors. Therefore, with improved metamaterial designs, these goals could be within reach in the near future.

8. 5 Summary of results

In conclusion, we have performed THz-TDS measurements on planar metamaterials with various dielectric overlayers. These data can be used to investigate the limitations and obstacles of using THz metamaterials as sensing devices. We have found that for our particular metamaterial design an overlayer of 100 nm is quickly approaching the limit of detectability. Our results are largely consistent with previous findings. However, measured results were not always in good agreement with simulations, particularly those involving very thin films (<200 nm). This strongly points to the necessity of experimental verification, not only to properly structure future simulations, but also to reveal the practical difficulties of analyte deposition on split-ring based sensors. Finally, our results illustrate many of the factors involved in sensing optimization, such as ring geometry, substrate composition, analyte composition and deposition, resonance effects, and limitations of the THz measurement system. Previous works have also discussed how some of these optimization variables might be utilized in future metamaterials and frequency selective surface based sensors. Such work presents a promising outlook for THz sensing technology.

CHAPTER IX

ELECROMAGNETICALLY INDUCED TRANSPARENCY (EIT) IN METAMATERIALS.

9. 1 EIT- A quantum phenomena

Electromagnetically induced transparency (EIT) is a coherent optical nonlinearity which renders a medium transparent over a narrow spectral range within an absorption line. Extreme dispersion is also created within this transparency window which also leads to slow light. Observation of EIT involves two highly coherent optical fields which are tuned to interact with three quantum states of the material. The probe field is tuned near resonance between two of the states and measures the absorption of the transition. A much stronger coupling field is tuned near resonance at a different transition. When the states are selected properly, the presence of the coupling field creates a spectral window of transparency which is detected by the probe as shown in Fig.. 9-1 [60]. The coupling laser is referred to as pump or control field.

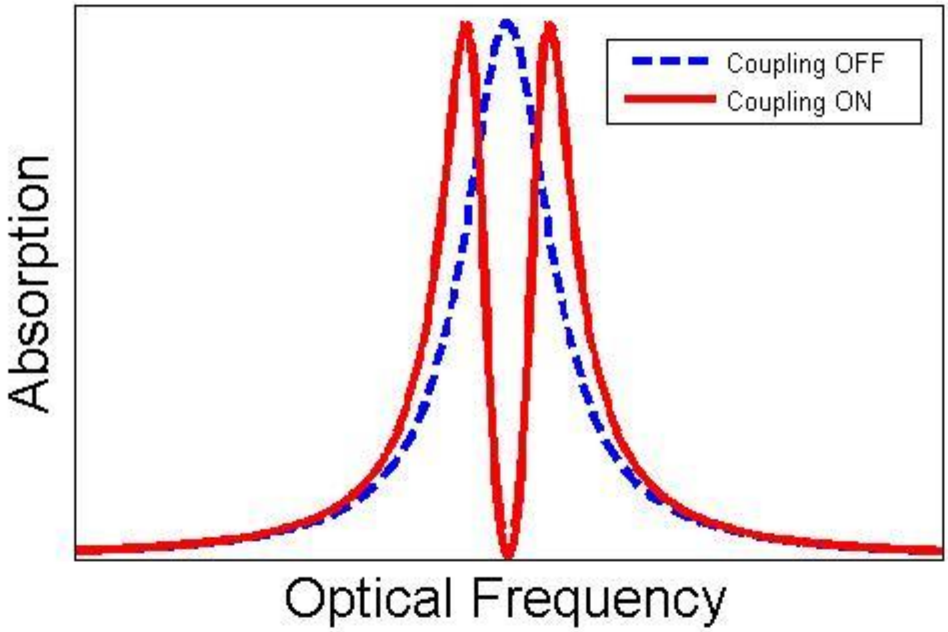

Figure 9-1. The effect of EIT on a typical absorption line. A weak probe experiences absorption shown as dotted blue line. A second coupling beam induces EIT and creates a window in the absorption region shown as the red solid curve [60].

9. 2 EIT in context of metamaterials

Metamaterials are a recently introduced novel class of artificial matter that is composed of, usually, periodically arranged unit cells. Their purpose is to control the properties of light propagation at will. This is accomplished by defining an appropriately tailored geometry for the unit cell. If the unit cells are sufficiently small, it is possible to homogenize the structure and attribute effective material parameters. To induce an effective electric and/or magnetic polarization that strongly deviates from that of a simple spatial average of the intrinsic material properties, resonances are usually evoked. Prominent examples for such unit cells are cut wire pairs or split ring resonators (SRR). At optical frequencies the resonances rely on the excitation of localized plasmon polaritons in the metallic structures forming the entities in the unit cell. At lowered wavelengths the same resonances persist, though then they should be rather understood on the base of an antenna effect. Once the fundamental mechanisms were revealed, sudden interest sparked on how the concepts of coupling between plasmonic eigenmodes can be exploited to sculpture the resonances of metamaterials in a more appropriate manner. Prominent examples are the application of the plasmon hybridization method [61,62] to explain the occurrence of magnetic atoms or even, more recently, magnetic molecule. Such investigations are usually driven by the desire to enlarge the bandwidth or to sharpen the resonances. As a rule of thumb one is inclined to believe that the sharper the resonance the stronger is the induced dispersion in the effective material parameters. Such resonance sharpening is extremely beneficial for obtaining low loss metamaterials. As the imaginary part of the material parameter decays off resonance faster than the real part, such sharp resonances would permit to choose an operating frequency for the metamaterial far away from the resonance position.

Potentially the most appealing approach to observe sharp resonances in coupled objects makes use of the excitation of a polaritonic resonance that is formed between a bright and a dark eigenmode [63,64]. For the purpose of coupling, the symmetry of the system has to be broken in order to allow the excitation of the dark state. Otherwise, it would have been forbidden. Speaking in terms of quality factors, the broken symmetry reduces the Q-factor of the dark state from infinity to a finite value. First investigations on such kind of systems were recently reported. They were designed to operate either at optical or at radio frequencies. Due to the apparent similarity to quantum interference in an atomic system comprising two indistinguishable paths, these investigations are usually regarded as a plasmonic analogy to electromagnetic induced transparency [63]. Whereas in such atomic system the spectral detuning of both resonances is understood as the principal feature that ultimately tailors the resonance, thus far no investigation was reported on how such detuning affects the coupled states in their plasmonic counterparts.

9. 3 Experimental design and measurement

We performed a systematic investigation of the impact of the relative spectral position of the involved resonances on the polaritonic coupled state and distinguished scenarios of weak coupling and strong coupling. For this purpose we focus on pairs of SRRs [65,66].

The length of the wires forming the SRR allows controlling the spectral position of the resonances in these systems; the spacing between the SRRs permits to tune the coupling strength in a controlled manner. The spectral response of appropriately and systematically designed samples is experimentally measured using a devoted THz time domain spectroscopy (THz-TDS) setup. Complementary rigorous numerical tools are employed to elucidate the effects theoretically. We have to stress that the main purpose of this investigation is to detail the phenomena occurring in the experimentally accessible spectral response from such structures. In consequence, no particular emphasis is put on the effective material parameters that could potentially be attributed to the medium.

The sample to be characterized is placed at the 3.5 mm diameter waist of the free space THz beam. Two sets of samples are fabricated using conventional photolithography on an n-type 640 µm thick silicon wafer with 12 Ω cm resistivity. Their general layout along with the definition of all geometrical quantities is shown in Fig. 9-2. The first set of samples, MM1-MM3 consists of touching SRRs. The section of the arm that both SRRs do share was merged into a single wire as evident from Fig. 9-2a, which represents the array of MM1. The second set of samples, MM4-MM6 comprises pairs of SRRs separated by a distance of s = 3 µm. Fig.s 9-2b and 9-2c show the schematic and the detailed definition of all geometrical parameters for MM4-MM6, respectively. The peculiarity of all the samples is the different position of the gap within the ring in both SRRs. Each set consists of samples in which the first SRR dimensions are fixed. The exact parameters of its geometry as revealed in Fig. 9-1c are g = 2 µm, w = 36 µm, l' = 36 µm, t = 6 µm, and h = 200 nm. The SRRs consist of vacuum deposited aluminum.

Within each set of samples all the geometrical parameters of the second SRR were kept identical except its arm length. The length parameter *l* was subject to variation and was set to be 36 µm, 51 µm, and 21 µm, respectively. The periodicity of the unit cells for all 6 structures is Λ_x = 50 µm by Λ_y = 100 µm. Each of the MM sample array has a 10 mm x 10 mm clear aperture and the THz wave illuminates the structure at normal incidence. The polarization of the electric field is chosen to be parallel to the gap of the first SRR. This conFig.uration allows to excite in the spectral domain of interest only an eigenmode in the first SRR. This eigenmode is bright and represents the lowest order odd mode. By contrast, the lowest eigenmode that can be excited for the second SRR appears at higher frequencies outside the spectral domain of interest at 1.33 THz. It is the lowest order even eigenmode. Nonetheless, this lowest order eigenmode is actually the second order one of the structure as the first order eigenmode appears to be dark and cannot be excited with the chosen polarization. The presence of the first SRR, however, breaks the symmetry and the mode becomes excitable. In the present investigation the arm length *l* that is subject to variation from sample to sample constitutes the parameter that permits to tune the spectral position of the dark relative to the bright mode. The separation *s* is the parameter that allows controlling the coupling strength between the both eigenmodes.

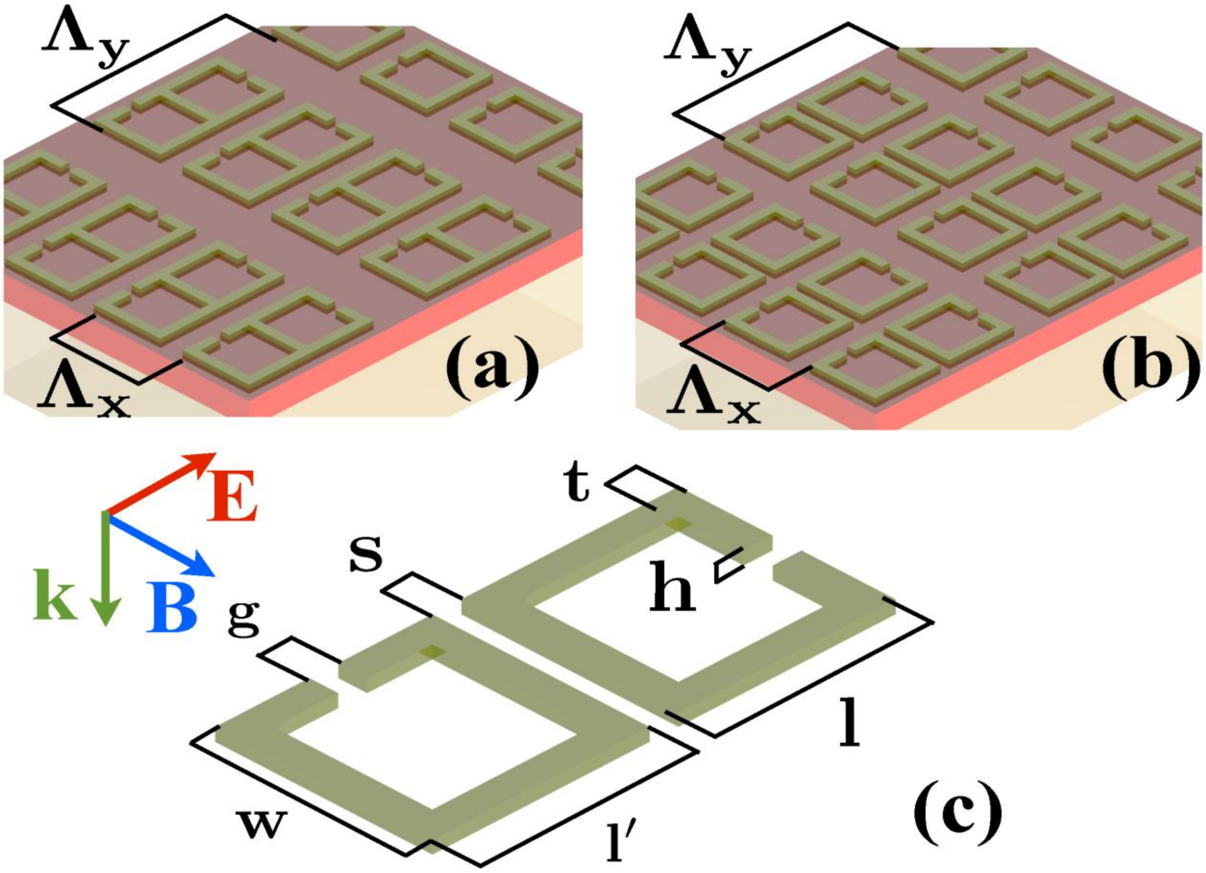

Figure 9-2. (a) Principal sketch of samples MM1 – MM3 where $s = 0$ μm and (b), principal sketch of samples MM4 –MM6 where $s = 3$ μm. (c) Detailed definition of the geometrical parameters at the example of the unit cells for MM4-MM6. They are chosen to be $t = 6$ μm, $g = 2$ μm, $l' = w = 36$ μm, $h = 200$ nm, $s = 3$ μm and l is subject to variations. The periodicity of the unit cells in all samples, MM1-MM6 is $\Lambda_x = 50$ μm by $\Lambda_y = 100$ μm.

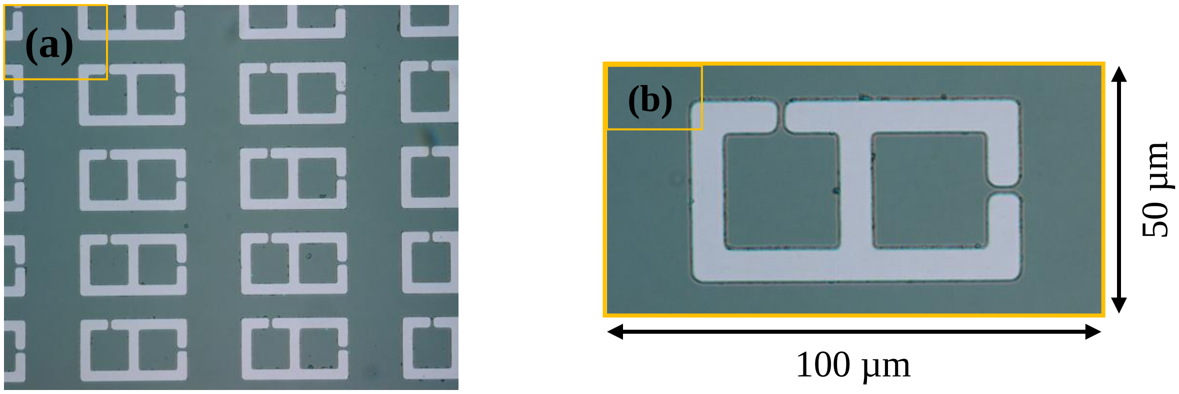

Figure 9-3. Microscopic image of (a) array and (b) Unit cell of MM1

Figure 9-4a shows the transmission spectra of the sample MM1. The unit cell of this sample contains two identical touching SRRs. The second SRR is rotated by 90 degrees with respect to the first one. The transmission spectrum is obtained by normalizing the measured transmission to the reference transmission of a blank n-type silicon wafer. Well pronounced resonances are difficult to resolve as the odd modes of the first SRR and the even modes of the second SRR are both excited with the chosen polarization. Consequently, the resulting spectrum consists of a series of closely spaced resonances that add up to such a weakly modulated spectrum, although the spectral positions of the resonances can be identified as weak dips. The only resonance that appears well pronounced occurs in the spectral domain of 0.4 to 0.6 THz. Figure 9-4b shows this spectral domain zoomed. From separate simulations it can be deduced that the resonance position coincides with the lowest order odd eigenmode that can be excited in the first SRR with the chosen polarization. However, we clearly observe a doublet rather than a single resonance, resulting in a transparency peak at 0.5 THz. From preliminary considerations we can deduce that the doublet occurs because of the strong coupling between the bright and the dark plasmonic eigenmode. For complementary purpose the Figures show also results from a rigorous numerical simulation of the experimental situation. Simulation is based on the Fourier modal method that takes into account the exact geometrical parameters, the dispersive permittivity of Al and the measurement procedure. We observe an excellent agreement in the entire spectral response that was simulated.

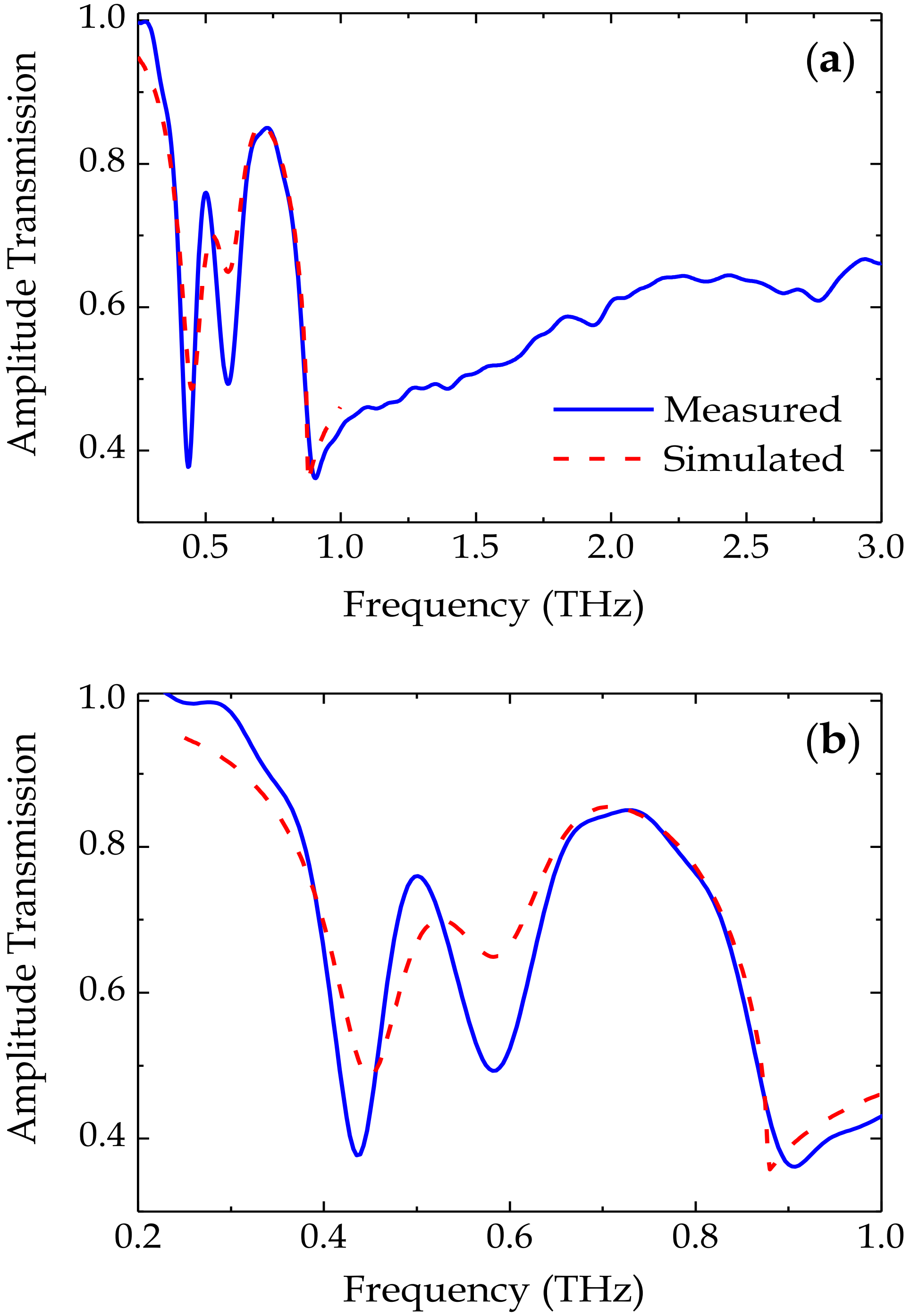

Figure 9-4. Measured and simulated amplitude transmission spectra of MM1 array which consists of touching SRRs with identical arm lengths. The incident E field is polarized parallel to the gap of the first SRR in the unit cell.

9. 4 Data Analysis

To elucidate this coupling in detail, Figure 9-5a shows the transmission spectrum of samples MM1-MM3, which is the case of the touching SRRs. The length *l* of the side arm of the second SRR for one sample was chosen such that for the isolated SRRs the resonance frequencies of the bright and the dark mode are the same. For the two other samples the dark mode appears at lower (higher) frequencies for a longer (shorter) length of its arms *l*. A pronounced and very strong spectral splitting of the bright mode is only observed for the sample where the wire length *l* of both SRRs is the same. The transparency peak at 0.5 THz is as high as 0.76. As the length of the second SRR is increased to 51 μm the dark eigenmode is excited at 0.37 THz. When the length is reduced to 21 μm in MM3, the dark eigenmode is shifted to the higher frequency of 0.77 THz. The excitation of the dark resonance is extremely weakened as soon as the size of the second SRR deviates strongly from the size of the first SRR. For comparison, Fig. 9-3b shows results of the simulated transmission for the samples MM1-MM3. Simulations are in perfect agreement with the experimental data of Figure 9-5a. All qualitative features are resolved and, to a certain extent, even quantitatively. The remaining discrepancies occur because of minor deviations in the dimensions of the fabricated sample geometry when compared to the design values that were considered in the simulations. From supportive simulation it can be seen that the spectra are sensitive against slight variations in the gap width *g* and the separation *s*.

Figure 9-5c shows the measured transmission spectrum of the 3 μm separated SRRs, MM4-MM6. Although difficult to resolve, the dark mode is weakly excited at 0.36 THz in sample MM5 ($l > l'$) and at 0.81 THz in sample MM6 ($l < l'$). The spectral separation of the two entities forming the doublet in sample MM4 ($l = l'$) is not as strong as for the touching SRRs. The numerically calculated spectrum is shown in Figure 9-5d. It is similarly in good agreement as the measurements.

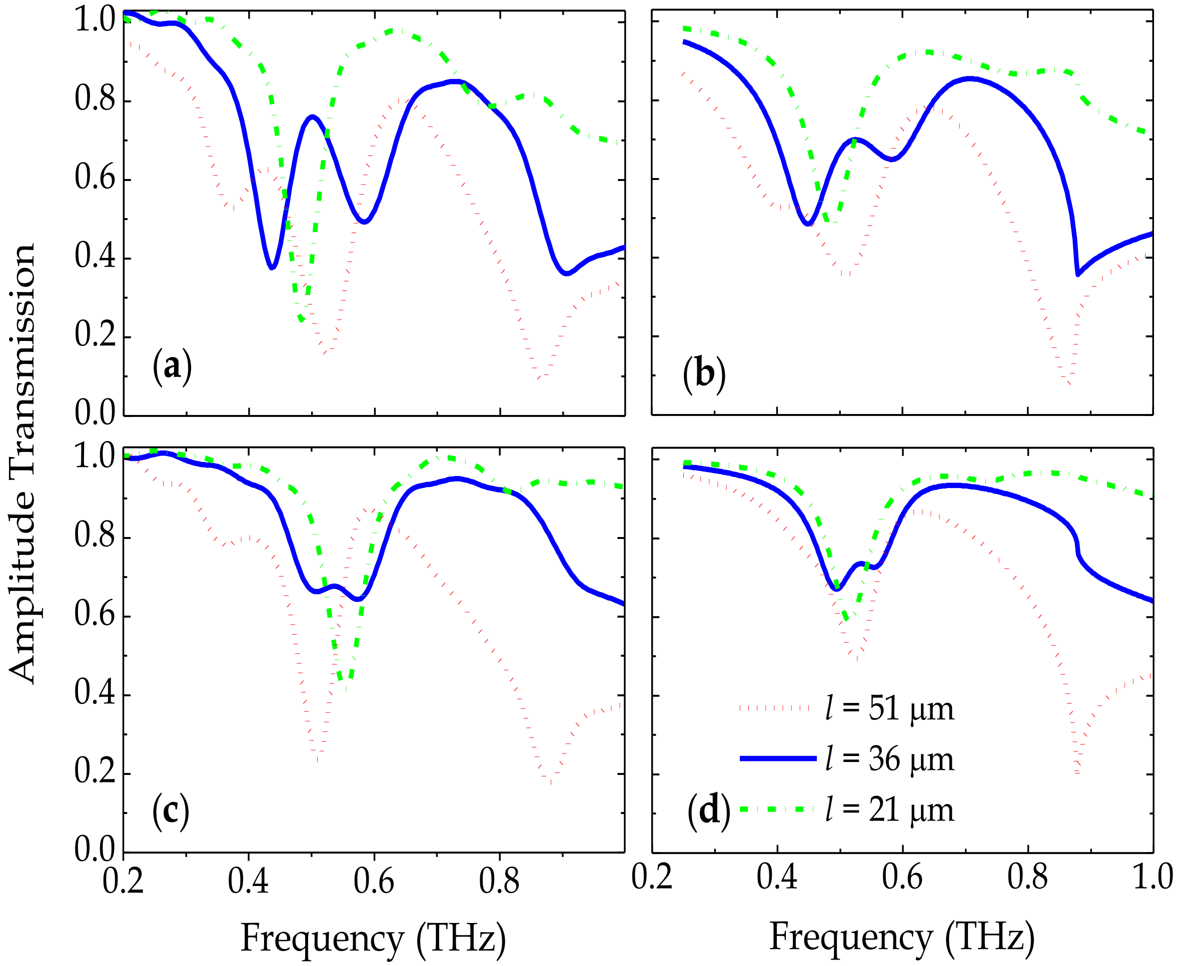

Figure 9-5. (a) Measured and (b) simulated amplitude transmission spectra of samples MM1-MM3. (c) Measured and (d) simulated transmission spectra of MM4-MM6.

9. 5 Simulation of transmission energy

Prior to discussing the results in detail, we show in Fig. 9-6a the color-coded simulated transmitted energy for the scenario where the two SRRs are touching. In the simulation the length parameter *l* is gradually increased from 15 to 50 µm, all the other geometrical parameters are set to be identical to their experimental counterparts. The extracted resonance positions are shown additionally (blue curve). The spectral position of the dark mode in the uncoupled scenario is likewise shown (green curve). The spectral positions were extracted from separate simulations of the same geometrical situation in the absence of the first SRR and a polarization of the incident electric field that was set to be parallel to the gap of the second SRR. This rotation of the incident polarization basically switches the eigenmode from being dark to bright. In passing we note that the spectral position of the bright mode remains constant and is evidently not affected by the variation of the wire length *l* of the second SRR. Fig. 9-6b shows the same results for the samples where the two SRRs are separated by 3 µm.

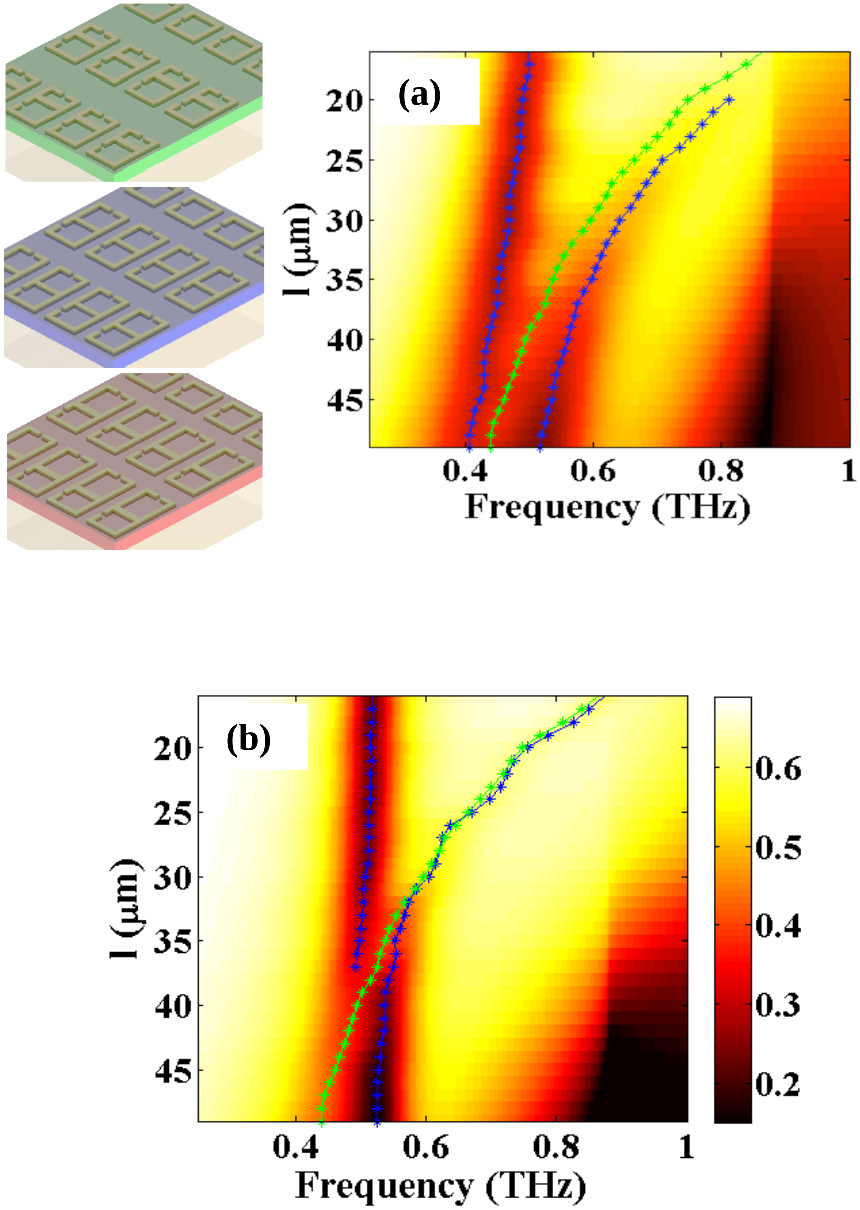

Figure 9-6. Simulated transmission of (a) touching SRRs and (b) 3 μm separated SRRs with the arm length *l* of the second SRR changes from 15 to 50 μm. The green curve is the resonance position of the second SRR with the E field polarized parallel to its gap as extracted from separate simulations. The blue curve is the resonance position of the excited eigenmodes extracted from the spectra.

9. 6 Discussion

From the experimental and the theoretical results we clearly observe a strong coupling between the bright and the dark plasmonic eigenmodes. Their interaction becomes possible because at a relative rotation by 90° the orientation of both SRRs breaks the overall symmetry of the coupled structure. This broken symmetry renders the excitation of the otherwise forbidden dark mode possible. However, due to their coupled nature the eigenmodes themselves are not excitable but rather a polaritonic state, which can be clearly seen from the simulated dispersion relation. For large spectral detuning of both resonances the excitation of the dark mode is rather weak; though traces in transmission remain evident. The closer the resonance frequencies get the stronger is the excitation of the dark mode. Similarly, the excited eigenmodes deviate from the spectral position of the eigenmodes for the isolated SRRs. Anticrossing causes a strong spectral separation of the bright and the dark mode from their spectral position in the unperturbed situation. We observe the excitation of a polaritonic state. A Rabi splitting of the energetic levels is experimentally observed and numerically verified for the case of the two touching SRRs. Such strong splitting renders the observed spectra to be similar to an Autler-Townes-like doublet. On the contrary, if the coupling between both resonances is significantly reduced (MM4-MM6 where the SRRs are separated by s = 3 μm) we do not observe sharp spectral features in the transmission spectra, neither in the experiments nor in the simulations. Although qualitatively, all features remain the same when compared to the case of two touching SRRs, the interaction of both SRRs is fairly weak. The weak coupling seems to be insufficient to induce sudden spectral changes, as one would expect in the case of a truly EIT analogy. The reduced coupling is caused by the reduced spatial overlap of the two eigenmodes. Because the eigenmodes are locally confined to the SRR, the probability to excite the dark mode is reduced in the broken symmetry conFig.uration for a large separation *s* of both SRRs. From the experimental and the theoretical data we can safely explain all spectral phenomena on the base of the plasmon hybridization model. Because of the broken symmetry the dark mode is bright. We assume that no significant deviation of its quality factor is encountered as compared to the bright mode. If both modes couple, a spectral splitting occurs. It leads to the formation of a symmetric and an anti symmetric mode. And finally the magnitude of the observed spectral splitting depends on the coupling strength between both eigenmodes.

9. 7 Summary of results

To summarize, our most important achievement in this work is to having elucidated the coupling between a dark and a bright plasmonic eigenmode in unit cells of MMs with broken symmetry. By increasing or decreasing the arm length of the second SRR the relative spectral position of both resonances can be controlled. It allows investigating the dispersion relation of the polaritonic state that is formed between the dark and the bright mode. It was observed that for a noticeable excitation of the polaritonic state the spectral positions of both states have to be sufficiently close. A significant coupling strength between both states leads then to a strong spectral splitting which in turn results in a transparency peak. The interaction between a dark and a bright mode in such broken symmetry unit cells adds a complementary aspect to the great variety offered by nanophotonics to tailor spectral resonances at will. Particularly in the field of MM it might lead to the development of broad band unit cells, low loss MMs or spectrally strong dispersive unit cells having a large effective group index.

CHAPTER X

CONCLUSION

The focus of this research has been to engineer the resonance properties of THz MMs for various applications like bio-sensing, negative refraction, sub wavelength antennas, and slowing down light. There were several impactful results obtained while probing into the exotic behavior of THz MMs.

Experimental work in the area of ultrathin meta films MMs gave insights into the critical metal film thicknesses at which the fundamental resonances of MMs show signs of evolution, gradual strengthening and saturation. This property can lead to the discovery of a passive THz modulators where the THz waves can be modulated just by varying the metafilm thickness of the MMs. An attempt to design an extremely high quality (*Q* factor) MM resonator was carried out by using high conductivity metafilms.

It was concluded in this experiment performed by us that the *Q* factor of these THz MMs saturates beyond a certain high conductivity of metals since the tremendous acceleration of electrons results in radiation losses which cannot be eleiminated for such thin metafilms.

Another route was followed to increase the *Q* factor of planar MMs where we used the concept of near field dipole coupling among SRRs by bringing them extremely close and obtaining a sharp resonant feature with '$Q = 19$' due to coherent coupling among the split ring resonators which is so far the highest among all existing planar THz MMs.

The sensing capabilities of MMs was demonstrated and proposed to be used for bio sensing applications by coating *nano* dimension thin film layers of DNA on the planar MMs. The sensitivity can be greatly enhanced if the quality factors of the planar THz MMs can be increased by orders of magnitude. This still remains a challenge to be worked on in future.

We also discovered a classical analog of the remarkable quantum phenomena, the electromagnetically induced transparency (EIT) through plasmonic coupling in THz MMs for the purpose of slowing down light.

The discoveries made in the area of THz MMs have added a whole lot to the present state of knowledge. The lack of THz components has always been a limitation for the development of full fledged THz devices for various applications. Our discoveries have definitely hastened the development of THz optics, imaging and sensing devices built on the principles of MMs. The MMs have also opened up the whole new field of designing optical antennas with desired response which were once only limited to lower frequencies. MMs have the potential to revolutionize the way light can be guided around an object, rather than reflect or refract. Our findings have established a strong connection towards the goal of finally creating cloaking devices. This technology for example can hide a stealth bomber sheathed by a layer of MMs and prevent its detection by radar. Finally, our research is a step forward towards building an optimized negative refractive index MM which will ultimately lead to the construction of a flat super lens with the ability to overcome the diffraction limit.

REFERENCES

1. V. G. Veselago, “The electrodynamics of substances with simultaneously negative values of ε and μ”, Usp. Fiz. Nauk **92**, 517 (1964) [Sov. Phys. Usp. 10, 509 (1968)].
2. J. B. Pendry, A. J. Holden, W. J. Stewart and I. Youngs, “Extremely low frequency plasmons in metallic mesostructures”, Phys. Rev. Lett. **76**, 4773 (1996).
3. J. B. Pendry, A. Holden, D. Robbins, and W. Stewart, “Magnetism from conductors and enhanced nolinear phenomena”, IEEE Trans. Microwave Theory Tech **7**, 2075 (1999).
4. D. R. Smith, W. J. Padilla, D. C. Vier, S. C. Nemat-Nasser, and S. Schultz, “Composite medium with simultaneously negative permeability and permittivity”, Phys. Rev. Lett. **84**, 4184 (2000).
5. K.Aydin, PhD Thesis, “Negative index metamaterials”, September 2004.
6. D. R. Smith, and N. Kroll, “Negative refractive index in left handed materials”, Phys. Rev. Lett. **85**, 2933 (2000).

7. R. A. Shelby, D. R. Smith, and S. Schultz, “Experimental verification of a negative index of refraction”, Science **292**, 5514 (2001).
8. J. Yao, Z. liu, Y. Liu, Y. Wang, C. Sun, G. Bartal, A.M Stacey, and X. Zhang, “Optical negative refraction in bulk metamaterials”, Science **321**, 930 (2008).
9. J. Valentine, S. Zhang, T. Zentgraf, E.U-Avila, D. A. Genov, G. Bartal, and X. Zhang, “ Three dimensional optical metamaterial exhibiting negative refractive index”, Nature **455**, 376 (2008).
10. S. Linden, C. Enkrich, M. Wegener, J. Zhou, T. Koschny, and C. M. Soukolis,“Magnetic response of metamaterials at 100 THz“, Science **306**, 1351 (2004).
11. T. J. Yen, W. J. Padilla, N. Fang, D. C. Vier, D. R. Smith, J. B. Pendry, D. N. Basov, and X. Zhang, “THz magnetic response from artificial materials”, Science **303**, 1494 (2004).
12. H. T. Chen, W. J. Padilla, J. M. O. Zide, A. C. Gossard, A. J. Taylor, and R. D. Averitt, “Active THz metamaterials”, Nature **444**, 597 (2006).
13. H. T. Chen, J. F. O’Hara, A.K. Azad, A. J. Taylor, R.D. Averitt, D.B. Shrekenhamer and W. J. Padilla, “Experimental demonstration of frequency-agile THz metamaterials,” Nature Photonics **2** ,295 (2008).
14. R. Singh, E. Smirnova, A. J. Taylor, J. F. O’Hara, and W.Zhang, “Optically thin THz metamaterials,” Optics Express **16**, 6537 (2008).
15. A. K. Azad, J. M. Dai, and W. Zhang, “Transmission properties of THz pulses through subwavelength double split ting resonators”, Opt. Lett. **31**, 634 (2006).

16. W. J. Padilla, A. J. Taylor, C. Highstrete, M. Lee, and R. D. Averitt, " Dynamical electric and magnetic metamaterial response at THz frequencies", Phys. Rev. Lett. **96**, 107401 (2006).
17. C. Caloz, and T. Itoh, " *Electromagnetic Metamaterials* ", Wiley, (2008).
18. D. Grischkowsky, S. Keiding, M. van Exter, and Ch. Fattinger, " Far infrared time domain spectroscopy of with THz beams of dielectrics and semiconductors", J. Opt. Soc. Am. B **7**, 2006 (1990).
19. A.K. Azad, "*Resonant THz transmission of plasmonic subwavelength hole arrays*", PhD thesis, (2006).
20. R. Marques, F. Mesa, Jesus Martel, and F. Median, "Comparative analysis of edge and broadside coupled split ting resonators for metamaterial design theory and experiments", IEEE Transactions on Antennas and Propagation **51**, 2572 (2003).
21. S. Ramo and J. R. Whinnery, "*Fields and waves in Modern Radio*", Wiley, New York, (1953).
22. A. K. Azad, Y. Zhao, and W. Zhang, "Transmission properties of THz pulses through ultrathin subwavelength silicon hole array", Appl. Phys. Lett. **86**, 141102 (2005).
23. J. W. C De Vries, "Temperature and thickness dependence of the resistivity of thin polycrystalline aluminum, cobalt, nickel, palladium, silver and gold films", Thin Film Solids **167**, 25 (1988).

24. M. Walther, D. G. Cooke, C. Sherstan, M. Hajar, M. R. Freeman, and F. A. Hegmann, “THz conductivity of thin gold films at the metal insulator percolation transition”, Phys. Rev. B **76**, 125408 (2007).
25. N. Laman, and D. Grischkowsky, “Reduced conductivity in the THz skin depth layer of metals”, Appl. Phys. Lett. **90**, 122115 (2007).
26. CST Microwave Studio ®, ©2005 CST-Computer Simulation Technology, Wellesley Hills, MA, USA.
27. P. Markos and C. M. Soukoulis, “Numerical studies of left-handed materials and arrays of split ring resonators”, Phys. Rev. E **65**, 036622 (2002).
28. Y. Zhao and D. R. Grischkowsky, “2-D THz Metallic Photonic Crystals in Parallel-Plate Waveguides”, IEEE Trans. Microwave Theory and Techniques **55**, 656, (2007).
29. M. A. Ordal , L. L. Long, R. J. Bell, S. E. Bell, R. R. Bell, R. W. Alexander, Jr., and C. A. Ward, “Optical properties of the metals Al, Co, Cu, Au, Fe, Pb, Ni, Pd, Pt, Ag, Ti, and W in the infrared and far infrared”, Appl. Opt. **22**, 1099 (1983).
30. K. Azad, Y. Zhao, W. Zhang, and M. He, “Effect of dielectric properties of metal on THz transmission subwavelength hole arrays”, Opt. Lett. **31**, 2637 (2006).
31. T. Thio, H.F. Ghaemi, H. J. Lezec, P. A. Wolff, and T. W. Ebbesen, “Surface-plasmon- enhanced transmission through hole arrays in Cr films,” J. Opt. Soc. Am B **16**, 1743 (1999).

32. N. C. Panoiu and R. M. Osgood, Jr.,“Influence of the dispersive properties of metals on transmission characteristics of left-handed materials”, Phys. Rev. E **68**, 016611 (2003).
33. R. Singh, C. Rockstuhl, F. Lederer, and W. Zhang, “The impact of nearest neighbor interaction on the resonances in THz metamaterials”, Appl. Phys. Lett., **94**, 021116 (2009).
34. L. Li, “New formulation of Fourier modal method for crossed surface-relief gratings“, J. Opt. Soc. Am. A **14**, 2758 (1997).
35. J. B. Pendry, D. Schurig, and D. R Smith, “Controllong electromagnetic fields”, Science **312**, 1780 (2006).
36. T. P. Meyrath, T. Zentgraf, and H. Giessen, "Lorentz model for metamaterials: Optical frequency resonance circuits", Phys. Rev. B **75**, 205102 (2007).
37. C. Rockstuhl, T. Zentgraf, C. Etrich, J. Kuhl, F. Lederer and H. Giessen, " On the reinterpretation of resonances in split ring resonators at normal incidence", Opt. Express **14**, 8827 (2006).
38. C. Dahmen, B. Schmidt, and G. von Plessen, "Radiation damping in metal nanoparticle pairs", Nano Lett. **7**, 318 (2007).
39. J. F. O’ Hara, R. Singh, I. Brener, J. Han, A. J. Taylor, and W. Zhang, “Thin film sensing with planar THz metamaterials: sensitivity and limitations”, Opt. Exp. **16**, 1786 (2008).
40. J. Gollub, T. Hand, S. Sajuyigbe, S. Mendonca, S. Cummer and D.R. Smith, “Characterizing the effects of disorder in metamaterial structures,” App. Phys. Lett. **91**, 162907 (2007).

41. M.V. Gorkunov, S.A. Gredeskul,I.V. Shadrivov and Y.S. Kishvar, “Effect of microscopic disorder on magnetic properties of metamaterials”, Phys. Rev. E **73**, 056605 (2006).

42. K. Aydin, K. Guven, N. Katsarakis, C.M. Soukoulis and E. Ozbay, “Effect of disorder on magnetic band gap of split ring resonator structures”, Opt. Exp. **12**, 5896 (2004).

43. R. Singh, A. Azad, A.J. Taylor, J. F. O’Hara, and W. Zhang, “Effect of metallic permittivity on resonant properties of THz metamaterials”, Opt. Lett. **33**, 1506 (2008).

44. R. Singh, E. Smirnova, A.J. Taylor, J.F. O’Hara, and W. Zhang, “Optically thin THz metamaterials,” Optics Express **16**, 6537 (2008).

45. P. H. Siegel, “THz technology in biology and medicine”, IEEE Microwave Theory Tech. **52**, 2438 (2004).

46. J. Barber, D.E. Hooks, D .J. Funk, R. D. Averitt, A. J. Taylor, and D. Babikov, “Temperature dependent far infrared spectra of single crystals high explosives using THz time domain spectroscopy”, J. Phys. Chem. A **109**, 3501 (2005).

47. J. Chen, Y. Chen, H. Zhao, G. J. Bastians, and X. C. Zhang, “Absorption coefficients of selected explosives and related compounds in the range of 0.1-2.8 THz”, Opt. Express **19**, 12060 (2007).

48. B. M. Fischer, M. Walther, and P. Uhd Jepsen, “ Far infrared vibrational modes of DNA components studied by THz time domain spectroscopy”, Phys. Med. Biol. **47**, 3807 (2002).

49. J. Zhang, and D. Grischkowsky, “Waveguide THz time domain spectroscopy of nanometer water layers”, Opt. Lett. **29**, 1617 (2004).

50. M. Nagel, P.H- Bolivar, M. Brucherseifer, H. Kurz, A. Bosserhoff, and Buttner, “Integrated planar THz resonators for femtomolar sensitivity label free detection of DNA hybridization”, Appl. Opt. **41**, 2074 (2002).

51. M. Nagel, F. Richter, P. H- Bolivar, and H. Kurz, “A funtionalized THz sensor for marker free DNA analysis”, Phys. Med. Biol. **48**, 3625 (2003).

52. C. K. Tang, J. Cunningham, C. Wood, I. C. Hunter, and A.G. Davies, “Electromagnetic simulation of THz frequency range filters for genetic sensing”, J. Appl. Phys. **100**, 066105 (2006).

53. T. Baras, T. Kleine-Ostmann, and M. Koch, "On chip THz detection of biomaterials: a numerical study", J. Biol. Phys. **29**, 187 (2003).

54. T. Driscoll, G. O. Andreev, D. N. Bosov, S. Palit, S. Y. Cho, N. M. Jokerst, and D. R. Smith, “Tuned permeability in THz split ring resonators for devices and sensors”, App. Phys. Lett **91**, 062511 (2007).

55. C. Debus and P. H- Bolivar, “Frequency selective surfaces for high sensitivity THz sensing”, App. Phys. Lett. **91**, 184102 (2007).

56. D. Qu, D. Grischkowsky, and W. Zhang, “THz transmission properties of thin subwavelength metallic hole arrays”, Opt. Lett. **29**, 896 (2004).

57. M. A. Cooper, Drug Discovery Today **11**, 1061 (2006).

58. SRU Biosystems, Inc., www.srubiosystems.com

59. Biacore Life Sciences, www.biacore.com

60. http://en.wikipedia.org/

61. E. Prodan, C. Radloff, N. J. Halas, P. Norlander, “A hybridization model for the plasmon response of complex nanostructures”, Science **302**, 419 (2003).
62. N. Liu, H. Guo, L. Fu, S. Kaiser, H. Schweizer, and H. Giessen, “Three dimensional photonic metamaterials at optical frequencies”, Nature Materials **7**, 31 (2008).
63. S. Zhang, D. A. Genov, Y. Wang, M. Liu, and X. Zhang, "Plasmonic induced transparency in metamaterials", Phys. Rev. Lett. **101**, 047401 (2008).
64. N. Papasimakis, V. A. Fedotov, N. I. Zheludev, and S. L. Prosvirnin, “Metamaterial analog of electromagnetically induced transparency”, Phys. Rev. Lett. **101**, 253903 (2008).
65. R. Singh, C. Rockstuhl, F. Lederer, and W. Zhang, “Coupling between a dark and a bright eigen mode in a THz metamaterial”, Phys. Rev. B **79**, 085111 (2009).
66. N. Liu, S. Kaiser, and H. Giessen, “Magneto inductive and electro inductive coupling in plasmonic metamaterial molecules”, Adv. Mat. **20**, 4521 (2008).

VITA

Ranjan Singh

Candidate for the Degree of

Doctor of Philosophy

Thesis: ENGINEERING THE RESONANCES OF TERAHERTZ METAMATERIALS

Major Field: Photonics (Electrical Engineering)

Biographical:

Personal Data: Born at Jamshedpur, India.

Education:

B.E. in Telecommunications, 2001, Bangalore University, India.
M. Tech in Optoelectronics and Laser Technology, 2004, Cochin University of Science and Technology, Kochi, India.
Completed the requirements for the Doctor of Philosophy in Photonics at Oklahoma State University, Stillwater, Oklahoma in August, 2009.

Experience:

Lecturer, RNSIT Bangalore, 2004 to 2005. Taught Physics to undergraduates as a teaching assistant from 2006 to 2009, also winning the Outstanding Teaching Assistant Award in 2008. Investigated terahertz metamaterials while working as a doctoral student under Dr. Weili Zhang at the Electrical Engineering department, Oklahoma State University from 2006 to 2009.

Professional Memberships: Student member of OSA, IEEE, and SPIE.

Name: Ranjan Singh Date of Degree: December, 2009.

Institution: Oklahoma State University Location: Stillwater, Oklahoma

Title of Study: ENGINEERING THE RESONANCES OF TERAHERTZ METAMATERIALS

Pages in Study: 120 Candidate for the Degree of Doctor of Philosophy

Major Field: Photonics (Electrical Engineering)

Scope and Method of Study:

The experimental tool used here in this investigation of terahertz metamaterials is a terahertz time domain spectrometer in which the transmitter and the receiver are photoconductive antennas driven and detected by femto second pulses. The terahertz pluse transmission through the different metamaterials was measured and analyzed by looking at the transmission spectrum and the phase change information. The metamaterial structures with minimum feature size of 2 μm were fabricated using conventional photolithography technique in a class 1000 clean room.

Findings and Conclusions:

The main findings in this research has been the unique behavior of sub-skin depth metamaterials, the critical thickness at which they start showing signatures of resonant features and then ultimately saturating at twice the skin depth of the metal used. They also show a direct conductivity dependent behavior but suffer from huge radiation losses when the metal acquires a superconducting nature. The near field coupling in metamaterials gives rise to sharp resonant features with high Q factor which has the potential to be used for thin film sensing. Dielectric over layers of as thin as 100nm shows a notable shift in the resonances of the metamaterial. Destroying the periodicity of metamaterials does not affect its resonance properties significantly. Asymmetric coupling scheme results in a sharp transparency peak which mimics the quantum phenomena of electromagnetically induced transparency.

ADVISER’S APPROVAL: Dr. Weili Zhang